Unraveling the Growth Mechanism of Magic-Sized Semiconductor Nanocrystals

Aniket S. Mule,[§,†] *Sergio Mazzotti,*[§,†] *Aurelio A. Rossinelli,*[†] *Marianne Aellen,*[†] *P. Tim Prins,*[‡] *Johanna C. van der Bok,*[‡] *Simon F. Solari,*[†] *Yannik M. Glauser,*[†] *Priyank V. Kumar,*[†,▽] *Andreas Riedinger,*[†,∥] *and David J. Norris*[*,†]

[†]Optical Materials Engineering Laboratory, Department of Mechanical and Process Engineering, ETH Zurich, 8092 Zurich, Switzerland

[‡]Condensed Matter and Interfaces, Debye Institute for Nanomaterials Science, Utrecht University, 3508 TA Utrecht, The Netherlands

[∥]Max-Planck-Institute for Polymer Research, Ackermannweg 10, 55128 Mainz, Germany

ABSTRACT: Magic-sized clusters (MSCs) of semiconductor are typically defined as specific molecular-scale arrangements of atoms that exhibit enhanced stability. They often grow in discrete jumps, creating a series of crystallites, without the appearance of intermediate sizes. However, despite their long history, the mechanism behind their special stability and growth remains poorly understood. This is particularly true considering experiments that have shown discrete evolution of MSCs to sizes well beyond the "cluster" regime and into the size range of colloidal quantum dots. Here, we study the growth of these larger magic-sized CdSe nanocrystals to unravel the underlying growth mechanism. We first introduce a synthetic protocol that yields a series of nine magic-sized nanocrystals of increasing size. By investigating these crystallites, we obtain important clues about the mechanism. We then develop a microscopic model that uses classical nucleation theory to determine kinetic barriers and simulate the growth. We show that magic-sized nanocrystals are consistent with a series of zinc-blende crystallites that grow layer by layer under surface-reaction-limited conditions. They have a tetrahedral shape, which is preserved when a monolayer is added to any of its four identical facets, leading to a series of discrete nanocrystals with special stability. Our analysis also identifies strong similarities with the growth of semiconductor nanoplatelets, which we then exploit to increase further the size range of our magic-sized nanocrystals. Although we focus here on CdSe, these results reveal a fundamental growth mechanism that can provide a different approach to nearly monodisperse nanocrystals.

INTRODUCTION

Colloidal quantum dots (cQDs) are nanometer-scale crystallites of semiconductor that have a quasi-spherical shape.[1] Because these nanocrystals confine charge-carriers (electrons and holes) in three dimensions, their opto-electronic properties depend strongly on their diameter.[1–3] For example, their fluorescence can be tuned across a broad spectral range, shifting to longer wavelengths as the nanocrystal size is increased. This has motivated the development of wet-chemistry protocols that can prepare cQD samples with a desired average size while maintaining a narrow size distribution.[4,5] Through these efforts, we can also now grow many nanocrystal shapes, such as quasi-one-dimensional nanorods[6] and quasi-two-dimensional (2D) nanoplatelets.[7,8] However, despite the tremendous control that nanocrystal protocols now offer, they cannot yield samples in which all nanocrystals are exactly the same size and shape (*i.e.* monodisperse).

In principle, this ideal limit is possible when the crystallites are extremely small, containing only a countable number of atoms.[9,10] In this molecular size regime, species referred to as "magic-sized clusters" (MSCs) have long been known.[11–13] They are believed to contain a precise ("magic") number of atoms arranged in a structure that exhibits superior stability compared to crystallites slightly smaller or larger. Furthermore, experiments indicate that, under the proper conditions, MSCs grow in discrete jumps, *i.e.* one magic size directly transitions to the next larger MSC in a series without the appearance of intermediate sizes. Consequently, MSCs could potentially offer a route to a family of monodisperse nanocrystals. Unfortunately, MSCs have typically been very limited in size (less than ~2 nm as estimated by sizing curves for cQDs[14]), consistent with the common belief that MSCs exist only at molecular scales.[11–13,15–19]

However, a few reports have begun to challenge this belief. Discrete growth of nanocrystals has been reported up to 3.5 nm,[20] leading to several interesting questions. While molecular-scale clusters may be expected to show special stability, what drives the appearance of larger MSCs? What are the size limits of MSC growth? More generally, what is the underlying formation and growth mechanism, and how does it differ from the process leading to conventional cQDs? Despite over three decades of nanocrystal research, these questions remain open due to our incomplete understanding of MSCs.

In part, progress has been impeded by experimental difficulties in the synthesis and analysis of these materials. Even for the most studied material, CdSe, typical MSC protocols produce crystallites that are hard to isolate and examine. Consequently, researchers have managed to successfully separate particles only below 2 nm. Samples containing larger MSCs typically contain multiple sizes simultaneously that have been challenging to isolate. Conventional characterization tools, such as transmission electron microscopy (TEM) and X-ray diffraction (XRD), also struggle to provide information at small sizes. In addition, unlike cQDs, MSCs do not typically exhibit "band-edge" fluorescence. If they did, such emission, which arises from electron–hole recombination at the effective band gap of the semiconductor nanocrystal, could provide further information about MSCs.

Despite these experimental challenges, models have still been developed that try to explain MSC growth. Typically, these involve one of three basic mechanisms: (i) fusion,[21–23] (ii) template-assisted

growth,[24–26] or (iii) layer-by-layer growth.[17,27] The first proposes that MSCs, irrespective of their size, can coalesce to form bigger MSCs. The second argues that a template is required to provide the required stability for MSC growth. The third hypothesizes that MSCs transition to the next size by adding a monolayer of semiconductor from the growth solution to the MSC surface. Crystallites with an incomplete monolayer represent kinetic transition states that cannot be observed or isolated. Using one of these three mechanisms, the existence of MSCs has been qualitatively rationalized. However, none of the models have been supported by detailed atomistic descriptions of the underlying processes. Although the stability of specific atomic arrangements observed in experiment has been theoretically justified,[28,29] no model has yet quantitatively explained how these arrangements arise and how they connect to other sizes in a series of MSCs.

To move toward a deeper understanding of MSCs, here we combine experiment and theory to examine the stability and growth of MSCs. We first present a synthetic protocol that extends CdSe MSCs to larger sizes (~2.7 nm as determined by electron microscopy). As this is beyond the "cluster" regime, we will now change to a more general term and refer to all species (from small to large) as magic-sized nanocrystals (MSNCs). Because our synthesis also allows these larger MSNCs to be isolated, challenges for standard characterization are reduced. Our experimental findings suggest that MSNCs grow as a series of crystallites with tetrahedral shape that transition from one size to the next by layer-by-layer growth. We then apply classical nucleation theory to develop a detailed microscopic model that can explain MSNC formation and growth. Using insights from this analysis, we show that our synthetic protocol can be extended to even larger CdSe MSNCs (~3.3 nm from electron microscopy). Together, our results offer a comprehensive and consistent picture of MSNCs. Moreover, because we do not limit the underlying chemistry, our model is applicable to other materials beyond CdSe. Thus, it extends our general understanding of nanocrystals.

RESULTS AND DISCUSSION

Synthesis and experimental characterization. Our synthesis utilizes the injection of bis(stearoyl) selenide into a heated solution of cadmium myristate in 1-octadecene, a non-coordinating solvent [see Section S1 in the Supporting Information (SI) for details]. This leads to the formation of CdSe products, which we can then characterize as a function of reaction time. For example, Figure 1a presents absorption spectra collected over 5 days for an injection and growth at 240 °C. For conventional cQDs, such spectra would reveal a continuous red-shift in the excitonic absorption features as the nanocrystal size gradually increased. For our reaction, the absorption peaks instead evolve in discrete jumps (see also Figure S1 in the SI). Indeed, our absorption spectra reveal 9 distinct product species. We denote each, as is common in nanocrystal research, by its longest wavelength absorption (excitonic) peak in nanometers. Thus, our 9 species are labeled as: 355, 380, 408, 434, 455, 476, 494, 508, and 523. (The last 7 of these are marked with vertical dashed lines in Figure 1a). During growth these species appear sequentially in this order. For example, the absorption peak at 434 nm (seen at 4 min in Figure 1a) slowly decreases with time while the next feature at 455 nm appears.[27] In addition, these transitions can be controlled through reaction time and temperature to target a specific MSNC size.

In the literature, such a discrete and sequential evolution of absorption peaks is usually assigned to a series of MSCs.[15,22,27,30] Typically, these series have been limited to peak wavelengths shorter than 450 nm.[23,27,31–34] When researchers tried to extend the growth to obtain features at wavelengths longer than 450 nm, the discrete jumps ended, and the peaks evolved continuously, as with cQDs. However, two synthetic protocols have been reported that produce discrete evolution of MSNCs beyond 450 nm, to 494 and 560 nm.[20,31] While our reaction conditions are different from these prior works, our protocol also allows growth to larger MSNCs, showing 5 additional product species beyond 450 nm. While this extension to longer wavelengths suggests formation of larger MSNCs, discrete evolution of absorption features during nanocrystal growth has also been assigned to other structures, such as nanoplatelets[7,8] and polymeric forms of CdSe.[35,36] Therefore, our products must first be isolated and characterized to determine if MSNCs are indeed present. Fortunately, our protocol allows isolation of specific species for analysis.

Therefore, we varied the reaction temperature and time to maximize the population of a desired product (Figures S1 and S2). This species was then selectively precipitated using an anti-solvent and subsequent centrifugation (see Section S1 in the SI for details). Using this procedure, we isolated four different products: 434, 455, 476, and 494. (The larger species, 508 and 523, were difficult to isolate in large yield from the reaction mixture that contained significant populations of multiple sizes.) Each of the isolated products was stored as a dispersion in hexane under ambient conditions. They retained their absorption features for at least four months, demonstrating their stability (Figure S3). Figure 1b,c plots the photoluminescence (PL) and absorption spectra, respectively, for 494 at room temperature. The PL spectrum displays both an intense narrow peak at 508 nm [with a full width at half maximum (fwhm) of 27.3 nm (130 meV)] and a much weaker, broad-band feature centered at ~700 nm. While the latter typically dominates the PL of MSCs[27,31,32,37] and is reminiscent of "deep trap" emission in cQDs,[38] the narrow peak is not commonly observed in MSCs. Its appearance is consistent with band-edge fluorescence. By monitoring the intensity of this narrow PL peak while scanning the excitation wavelength, photoluminescence excitation (PLE) spectra can be obtained and compared with absorption results (Figure 1c).[39,40] The strong similarity between the two spectra confirms that the narrow PL peak arises from the same species that leads to the absorption features. Taken together with PL and PLE results for the other isolated 434, 455, and 476 species (Figure S4), which exhibit narrow PL peaks at 450, 474, and 492 nm, respectively, we conclude that we have isolated four nanocrystal sizes that exhibit band-edge fluorescence. Combined with their discrete growth, this suggests that our 9 product species represent a series of MSNCs of increasing size.

To test this further, we turned to TEM and scanning TEM (STEM) to probe the size and shape of these isolated products. As mentioned above, small species can be challenging to characterize. This remains true even for our larger isolated MSNCs, which are susceptible to beam damage and exhibit limited contrast. Nevertheless, images of our 494 sample using high-angle annular dark-field (HAADF) STEM clearly show particles (Figure 1d). On the TEM grid, they spontaneously organize into ordered assemblies, indicating particle uniformity. We observed similar assemblies for our other isolated products (Figure S5). Unlike reports where particles were trapped in lamellar templates or fibrous

assemblies,[24–26,41] our images reveal particles well separated from each other (a center-to-center distance of ~4.9 nm was extracted from Figure 1d). While the images suggest that the particles are faceted (discussed further below), the crystallites do not exhibit strong shape anisotropy, eliminating nanoplatelets or CdSe polymers as possible species.[8,35,36] Furthermore, the particle size is well below the exciton Bohr radius of CdSe (5.6 nm), indicating that the discrete jumps observed in the optical spectra indeed come from changes in the carrier confinement as the particle size increases. By analyzing images from the 434, 455, 476, and 494 samples in more detail we extracted average effective diameters of 2.1±0.3, 2.4±0.4, 2.6±0.3, and 2.7±0.4 nm, respectively, where we have listed standard deviations for thousands of particle measurements (Figure S6). Thus, the products are increasing in size, consistent with a series of MSNCs.

The apparent faceted nature of the particles suggests deviation from a quasi-spherical shape. However, a detailed investigation by electron microscopy was prevented by fast shape evolution under the electron beam (Figure S7). The crystallinity of the species could be confirmed by powder XRD. Figure 1e shows the diffractogram for the 494 sample. While the peaks are broadened as expected due to the small particle size, the strong single diffraction peak at ~26° without reflections at ~35° and ~46° indicates that these particles have the zinc-blende crystal structure. This eliminates the possibility that these larger MSNCs have closed-cage or tubular-pair structures, as discussed earlier based on mass spectrometry[16] and XRD experiments.[42] Instead, our results are more consistent with the tetrahedral shape previously proposed.[17,32] This is supported by the isotropic and faceted nature of our particles in electron microscopy. Furthermore, the smallest species that we observe (355) was previously determined to be tetrahedral by measuring single-crystal XRD on crystals of MSCs.[32]

The analysis above implies that MSNCs form as a series of tetrahedral-shaped crystallites that grow from one size to the next in a discrete and sequential manner. With the zinc-blende lattice, these tetrahedra would expose four identical {111} facets. However, their growth mechanism still remains unclear. Further information can be gained by considering the synthetic protocols that have led to MSNCs instead of cQDs. In general, MSNC syntheses have utilized reactive precursors.[20,23,32,33,43,44] Indeed, our selenium and cadmium precursors [bis(stearoyl) selenide and cadmium myristate], which enter the reaction in their reduced (Se^{2-}) and oxidized (Cd^{2+}) forms, quickly combine to generate CdSe "monomers."[45] (We note that the composition of these monomers is poorly understood. For simplicity, we assume a CdSe atomic pair.) The fast generation of CdSe monomers from the reaction of bis(acyl) selenides (sulfides) and cadmium carboxylates was previously utilized to form CdSe (CdS) nanoplatelets.[45,46] To assess the importance of highly reactive Se precursors for MSNCs, we repeated our reaction with two less-reactive Se precursors that are often exploited in nanocrystal syntheses, elemental Se and trioctylphosphine selenide (Figure S8). Neither produced MSNCs. These experiments, in agreement with previous reports,[20,23,32,33,43,44] suggest that highly reactive precursors are required for the formation of MSNCs.

Growth in the absence of precursor. With highly reactive precursors, a near-instant reaction of the limiting reagent, the Se precursor, would be expected. Assuming that the Se precursor is consumed to produce monomers, this implies that MSNCs grow under conditions in which the reactive Se

precursor is absent. To test this hypothesis, we isolated 434 and heated this species for 22 h at 180 °C in a solution of only cadmium myristate in 1-octadecene (Figure 2a). The absence of bis(stearoyl) selenide was confirmed by ^{1}H nuclear magnetic resonance (NMR) spectroscopy (Figure S9). Nevertheless, our isolated 434 still evolved discretely to 455 and then 476. We conclude that MSNC growth does not require the reactive Se precursor to be present.

Furthermore, this experiment with isolated 434 provides valuable information for distinguishing the previously proposed growth mechanisms: (i) fusion,[21–23] (ii) template-assisted growth,[24–26] and (iii) layer-by-layer growth.[17,27] The growth of an isolated MSNC to the next bigger size is difficult to explain through fusion.[21–23] The isolation presumably removes monomers and any smaller particles that might be present. Thus, fusion would require the combination of two 434 species, which would immediately lead to a size larger than 455. As this is not observed, we eliminate fusion as the mechanism for MSNC growth. A template-assisted mechanism could in principle occur if the isolated MSNCs then become trapped in lamellar templates or fibrous assemblies. This would require either the cadmium myristate or the 1-octadecene to form these templates. However, our electron micrographs show no evidence of particles trapped in such templates (Figure 1d). In addition, previous reports have shown that cadmium carboxylates do not form molecular mesophases under our reaction conditions.[47–49] While the polymerization of 1-octadecene has recently been discussed,[50] its role as a possible template can also be excluded based on solvent-free experiments, discussed below. Thus, we also reject template-assisted growth for our MSNCs.

The evolution of our isolated 434 appears to be more in line with layer-by-layer growth,[17,27] in which MSNCs transition to the next size by addition of a monolayer of monomers. As our MSNCs grow sequentially even without Se precursors, this implies that any monomers that are present must be produced from the MSNCs themselves. Monomers can be generated because the solution is initially below the solubility concentration of the crystallites. Therefore, we propose that a fraction of the MSNCs dissolve, providing monomers for the growth of the remaining particles. Such a process has already been invoked to explain ripening of CdSe nanoplatelets.[46,51] For the MSNCs, these monomers add to one of the facets of the tetrahedral-shaped particles and complete a layer to form the next bigger size. Note that the addition of a layer to any of the four facets of a tetrahedron results in the next bigger tetrahedron in a series, consistent with MSNC growth.

The above growth mechanism would involve two processes: (i) diffusion of monomers between the solution and the MSNC surface and (ii) surface reactions that add or remove these monomers. If diffusion is the rate-limiting step, the addition of an arriving monomer to the growing crystallite by a surface reaction is fast in comparison. After one monomer joins, a second monomer can add to the same monolayer (layer-by-layer growth) or to a new monolayer on top (multi-layer or rough growth). While these two surface reactions might have different kinetics, their overall rates (diffusion followed by surface reaction) will be almost the same when diffusion is limiting. Consequently, both can occur with similar probability. Thus, for layer-by-layer growth to occur, the mechanism must instead be surface-reaction limited.[49] In general, this is more likely if the molecular ligands that passivate the crystallite surface are present at high concentrations.[49,52,53] Excess ligands can impede the attachment/detachment

of monomers. We investigated this by comparing reactions with two different concentrations of our ligand, cadmium myristate.[54,55] When isolated MSNCs were heated with no ligand, discrete growth did not occur (Figure S10). However, when the MSNCs were heated with only ligand (*i.e.* without solvent), discrete growth was observed from 434 to 455, 476, and larger (Figure 2b). The appearance of discrete growth at high cadmium myristate concentration without solvent suggests that MSNCs grow under surface-reaction-limited conditions. (It also eliminates the possible involvement of any template formed from polymerized ODE in MSNC growth, as mentioned above.)

Modelling the stability and layer-by-layer growth of MSNCs. We now develop a microscopic theory that can explain the above experimental observations. Our model must resolve why MSNCs are especially stable, why they grow discretely and sequentially, and why the growth is sufficiently controllable to isolate a MSNC size in the series. For this, we use classical nucleation theory to describe the stability of tetrahedral-shaped crystallites. In general, classical nucleation theory describes the energy change associated with the transfer of a given number of monomers—in our case CdSe—from solution to a three-dimensional (3D) particle. For a tetrahedral-shaped crystallite, the Gibbs free energy of formation, $\Delta G^{3\mathrm{D}}$, is given by[56]

$$\Delta G^{3\mathrm{D}}(n) = -\Phi(n)\Delta\mu + 4\varepsilon_A\Gamma(n) \quad (1)$$

where n corresponds to the number of monomers per edge of the tetrahedron (see Figure 3a), $\Phi(n)$ is the tetrahedral number that describes the number of monomers in the entire MSNC, and $\Gamma(n)$ is the triangular number that represents the number of monomers on a triangular MSNC facet. [For a MSNC with 5 monomers on the edge (n=5; Figure 3a), the tetrahedral and triangular numbers are equal to 35 and 15, respectively.] $\Delta\mu$ is the supersaturation that quantifies the chemical-potential difference between a monomer in solution and in the bulk crystal, and ε_A is the energy required to break a crystalline bond and passivate it with a ligand. ε_A relates to the surface energy (σ_A) as $\varepsilon_A = \sigma_A\rho_A$, where ρ_A is the surface area per dangling bond. For simplicity we will refer to ε_A as the surface energy. Here we use ε_A = 128 meV for the relevant Cd-terminated and passivated {111} surfaces of CdSe.[57] See Section S3.1 in the SI for further details. We note that, in our notation, $\Delta\mu$ and ε_A are positive quantities. Consequently, the first term in eq 1 is negative (due to formation of bulk crystal) and the second term is positive (due to formation of surface).

Eq 1 is plotted in Figure 3b. Whether a MSNC is stable (and grows) or unstable (and dissolves) is determined by the balance of the two terms, *i.e.* the surface-to-volume ratio of the crystallite. Expressed differently, it depends on the 3D critical size—the size that represents the maximum in the energy-of-formation curve (eq 1) for a fixed supersaturation (Figure 3b). For MSNCs smaller than the 3D critical size, the energy of formation increases with increasing size, and these MSNCs tend to dissolve. The opposite is true for MSNCs larger than the 3D critical size, which tend to grow.

Our experimental results discussed above suggest that MSNCs grow layer by layer. In this regime,[17,27] crystallites increase in size through the formation and growth of a 2D surface island that ultimately covers an entire crystal facet. Due to the tetrahedral shape of MSNCs, covering any of the four identical facets yields the next bigger tetrahedron. Therefore, we propose that transitioning from

one MSNC size to the next occurs through the formation of a 2D surface island on one of its facets. The free-energy change associated with the formation of such a 2D island is

$$\Delta G^{2D}(m) = -\Gamma(m)\Delta\mu + 4\varepsilon_A m + \varepsilon_S m \quad (2)$$

where m corresponds to the lateral number of monomers forming the 2D island (see Figure 3a), and $\Delta\mu$ and ε_A are defined as in eq 1. The step energy (ε_S) accounts for the fact that monomers located at the step edge (Figure 3a) cost an additional energy compared to monomers located on a terminated facet (ε_A).[49,51] In our calculations we assume $\varepsilon_S = 5\varepsilon_A$ (see Section S3.2 in the SI for details).

Eq 2 is plotted in Figure 3c. Just as we did for the 3D crystallite, we can define a critical size for the growing 2D island. For islands smaller than this size, dissolution of the island is thermodynamically favored (Figure 3c). In contrast, when it is larger than the 2D critical size, a thermodynamic driving force exists for growth.

However, so far, we have not considered that the growing 2D island eventually covers the underlying facet. When this occurs, we must account for the disappearance of the step edge (Figure 3a), which leads to a sudden decrease in the free energy. This effect could be particularly important for facets smaller than the 2D critical size. In that case, the energy barrier for growth would be below that for a bulk crystal, as previously seen for CdSe nanoplatelets.[49,51] This is the reason why in nanoplatelets the growth barrier was found to decrease with decreasing facet thickness. Thus, the disappearance of a step edge played a critical role in understanding nanoplatelet growth, and it must be included in our model for MSNCs.

This can be accomplished by simply dropping the last term (the step energy) in eq 2 when the facet is completed, *i.e.* when $m = n + 1$ (see Figure 3a). $\Delta G^{2D}(m)$ can then be written as

$$\Delta G^{2D}(m) = \begin{cases} -\Gamma(m)\Delta\mu + 4\varepsilon_A m + \varepsilon_S m & \text{if } m < n+1 \\ -\Gamma(m)\Delta\mu + 4\varepsilon_A m & \text{if } m = n+1 \end{cases}. \quad (3)$$

Then, the overall formation energy of a MSNC with a 2D island growing on it is

$$\Delta G(n,m) = \Delta G^{3D}(n) + \Delta G^{2D}(m)\,, \quad (4)$$

where *n* is the lateral size of the initial MSNC and *m* is the lateral size of the additional 2D island. Note that by construction $\Delta G(n, n+1) = \Delta G^{3D}(n+1)$ and $\Delta G(n, 0) = \Delta G^{3D}(n)$.

Now armed with eq 4, we can generate a quantitative description of the energy of different sizes of MSNCs and the transition states that link them. For our first discussion, we assume fixed supersaturation ($\Delta\mu$). The formation energy of MSNCs [$\Delta G(n, 0)$] as a function of their lateral number of monomers (n) can then be determined (blue circles in Figure 3d). These different MSNCs are connected through energy barriers that are governed by the formation of a 2D island on their facets. These processes are represented by red lines in Figure 3d. The discontinuities in these energy-of-formation curves arise due to the sudden disappearance of the step edge, *i.e.* at the moment the island has fully covered the facet. Figure 3d also clearly shows that, for MSNCs with facets smaller than the 2D critical size ($n < 5$), the barriers connecting them are size dependent. In contrast, the energy barriers connecting MSNCs with facets larger than the 2D critical size ($n \geq 5$) are size-independent and are

equivalent to growth barriers on a bulk facet. (See also Figures S11 and S12 in the SI for other parameter choices.) These findings indicate that the discrete evolution of MSNCs shares similarities to the growth of nanoplatelets.[49,51] Our results also reveal that MSNCs correspond to local minima in the energy-of-formation curve and show that the transition states that link them are thermodynamically unstable. Contrary to the conventional picture held, which attributes the superior thermodynamic stability of MSNCs to a "magic" number of atoms that appears arbitrary, we propose that it is the tetrahedral shape, small size, and layer-by-layer growth under surface-reaction-limited conditions that determine the special behavior of MSNCs.

The above model can in principle explain the discrete and sequential growth of MSNCs. It predicts specific sizes that are stable with kinetic barriers between them. This rationalizes why MSNCs grow discretely. The sequential growth can be understood using the following simple example. Suppose two MSNCs that are one size apart co-exist. If the growth barriers are size independent, both have equal probability to grow to the subsequent size. Then, as both grow, we would expect the disappearance of the smaller MSNC to correlate with the appearance of the new, larger MSNC. In contrast, if the barriers are size-dependent (increasing with size), the smaller-sized MSNC is more likely to grow than the larger one. In this scenario, one would expect the smaller MSNC to grow before the larger-sized one does, in line with the sequential growth observed in experiments. We note that this "size-focusing" process is different than the mechanism previously discussed for diffusion-limited growth.[58,59] In our case, the number of discrete sizes is focused due to the nature of the kinetic barriers between MSNCs under surface-reaction-limited conditions.

Our model therefore suggests that discrete and sequential growth of MSNCs requires two criteria to be satisfied. The 3D crystallite must be stable (larger than the 3D critical size), and the barrier for 2D island growth must be smaller than on a bulk surface (to obtain size-dependent barrier heights). The size regime where these two criteria are simultaneously satisfied is represented by the beige-shaded region in Figure 3b-d. Clearly, this region is too narrow to explain the 9 MSNC species observed during our synthesis.

Growth dynamics. This inconsistency between the model and experiment can be resolved by considering the dynamics of MSNC growth.[51] This involves accounting for changes in the supersaturation ($\Delta\mu$) due to monomer depletion as the formation and subsequent growth of MSNCs proceed. Changes in $\Delta\mu$ affect the overall energy-of-formation curve (eq 4), which in turn influences both the MSNC stability and the barriers between sizes. Thus, the situation in a real experiment is more complicated than that depicted in Figure 3d.

The influence on MSNC stability can be described through a 3D critical supersaturation $\Delta\mu_{n,\mathrm{crit}}^{\mathrm{3D}}$ (where *n* again is defined as in Figure 3a), which represents the supersaturation at which MSNCs of a given size become unstable and directly correlates with their solubility. When the supersaturation is larger than $\Delta\mu_{n,\mathrm{crit}}^{\mathrm{3D}}$, MSNCs of lateral size n are stable and tend to grow. In contrast, the same MSNCs dissolve when the supersaturation is smaller than $\Delta\mu_{n,\mathrm{crit}}^{\mathrm{3D}}$. The influence on the barriers between sizes

can be similarly described using $\Delta\mu^{2D}_{m,crit}$, the 2D critical supersaturation corresponding to a 2D critical island of lateral size m.

Figure 4a presents these quantities in terms of supersaturation *versus* size in a stability diagram for MSNC growth. The blue curve represents $\Delta\mu^{3D}_{n,crit}$. Above this line, MSNCs of lateral size n are stable; below they are unstable. The red curve plots $\Delta\mu^{2D}_{n+1,crit}$ as a function of *n*. [Note that $\Delta\mu^{2D}_{n+1,crit}$ is shown instead of $\Delta\mu^{2D}_{n,crit}$ because the facets of MSNCs of size *n* are covered by 2D islands one larger in lateral size (see Figure 3a).] Below this red curve the barriers are size dependent; above they are size independent. If we consider a horizontal slice through Figure 4a (*i.e.* at fixed $\Delta\mu$), the beige region between the blue and red curves defines the size regime where the two criteria for MSNC growth are satisfied: MSNCs are stable and exhibit size-dependent barriers. However, as the supersaturation decreases with time, the barriers linking different MSNCs increase. This is because the first term in eq 3 is less negative as $\Delta\mu$ falls. Consequently, the size range for which MSNCs exhibit size-dependent barriers shifts towards larger sizes (see beige region in Figure 4a). Simultaneously, the size of MSNCs that are unstable and dissolve (blue region) increases. These trends are summarized in Figure 4b, which shows the barriers and stability associated with different MSNC sizes for two different constant supersaturations (200 and 280 meV).

We can incorporate all of these effects in a population-balance model to simulate MSNC growth. The approach is similar to that previously applied to nanoplatelets.[51] For MSNCs, we connect different sizes in a cascade-type model, as depicted in Figure 4c. In line with our experiments, we assume that growth and dissolution occur layer by layer through the addition or removal of one monolayer. Each MSNC size can then either grow to the next-larger MSNC (consuming monomers) or dissolve to the next-smaller MSNC (generating monomers). The growth rate (I_n) for MSNCs of lateral size n to increase to size n + 1 is then determined by the barrier for growing a 2D island that covers a MSNC facet, *i.e.*

$$I_n = C\exp\left[-\frac{E_{n,barr}}{k_B T}\right], \tag{5}$$

where C is the attempt frequency, k_B is the Boltzmann constant, T is the reaction temperature, and $E_{n,barr}$ is the barrier to transition to the subsequent MSNC species (see Section S4 in the SI for details). Similarly, the size-dependent solubility determines the rate at which MSNCs dissolve to the next-smaller size. An expression for the dissolution rate, D_n, is obtained by imposing an equilibrium condition. At the equilibrium supersaturation $\Delta\mu^{3D}_{n,crit}$ the growth and dissolution rates are the same:[51]

$$D_n = I_{n-1}(\Delta\mu^{3D}_{n,crit})\,. \tag{6}$$

The monomer concentration and the supersaturation are linked through $\Delta\mu = k_B T\ln(\tilde{c}_1)$, where $\tilde{c}_1$ is the monomer concentration normalized so that $\Delta\mu = 0$ corresponds to the bulk solubility. In our model, only the smallest MSNC size (n = 2) is assumed to form directly from the monomer solution. Temporal changes in the monomer concentration (and therefore $\Delta\mu$) due to growth and dissolution of MSNCs are accounted for by imposing mass balance on the overall system.

In our simulation, the conversion of precursors to monomers is assumed to occur instantaneously, which agrees with the high precursor reactivity observed in experiment. This provides an initial supersaturation that is greater than the solubility of all possible MSNC sizes. However, the supersaturation quickly drops within the range for which the barriers connecting different MSNCs of size n = 2 and 3 are size-dependent ($\Delta\mu$ ~330 meV). Figure 4d plots the supersaturation *versus* normalized reaction time τ on a logarithmic scale. The vertical lines indicate when $\Delta\mu$ decreases below the blue curve in Figure 4a for $n = 2$, 3, and 4. In other words, they indicate when these sizes become unstable and start to dissolve. Figure 4e shows the temporal evolution of different MSNC populations in terms of monomer fraction. Here, vertical arrows indicate the moment $\Delta\mu$ falls below the red curve in Figure 4a for $n + 1 = 3$, 4, 5, and 6, indicating when species with $n = 2$, 3, 4, and 5 enter the beige area. For each species, the vertical arrow therefore marks the time point when the barrier to transition to the next-larger size becomes smaller than the growth barriers on a bulk facet, *i.e.* size dependent.

Our simulation results, summarized in Figure 4e, explain how controlled sequential growth of MSNCs can occur. Namely, the population of the $n = 2$ species rises early as it consumes monomer. It then transitions to the $n = 3$ species, followed by the sequential appearance of $n = 4$, $n = 5$, *etc*. Figure 4e also displays an important correlation. When the supersaturation in solution, $\Delta\mu$, approaches the 2D critical supersaturation, $\Delta\mu^{2\mathrm{D}}_{n+1,\mathrm{crit}}$ (see vertical arrows), the corresponding monomer fraction of MSNC species n reaches a maximum and then decreases drastically. This suggests that the supersaturation determining the barrier height to transition from MSNC species of lateral size n to $n+1$ is approximately $\Delta\mu^{2\mathrm{D}}_{n+1,\mathrm{crit}}$. As shown by the red curve in Figure 4a, the 2D critical supersaturation decreases with increasing MSNC size. Decreased supersaturation implies larger barriers connecting two subsequent species (see Figure 4b) which, in turn, explains the logarithmic times observed in the growth dynamics. As a result, smaller MSNCs grow faster than larger ones. At the same time, small MSNCs also exhibit the highest solubility, and, thus, are the first to dissolve as the supersaturation decreases. They then generate monomers that are consumed by larger MSNCs, which remain stable.

Extending the size range. The growth mechanism of MSNCs discussed here shows many parallels to that of nanoplatelets. Both mechanisms rely on size-dependent growth barriers that occur during layer-by-layer growth under surface-reaction-limited conditions. This results in controlled sequential growth between a series of nanoplatelets of increasing thickness or MSNCs of increasing size. However, clear differences also exist. Nanoplatelets have two types of distinct facets, narrow side facets where the growth occurs and wide top and bottom facets where no growth occurs. Consequently, nanoplatelets do not increase in thickness by adding a monolayer to the wide facet (as one might naively expect). Rather, nanoplatelets of increasing thickness appear and disappear due to lateral expansion of small nuclei followed by lateral dissolution.[46,49,51]

Nevertheless, the similarities between the mechanisms for MSNCs and nanoplatelets suggest that synthetic strategies that have extended the thickness range of nanoplatelets could similarly impact the achievable size range of MSNCs. In particular, previous studies have shown that thicker nanoplatelets can be grown when chloride (or a halide more generally) is added to standard nanoplatelet protocols.[60–

[62] While the explanation is still debated, the surface energy of the exposed {100} facets on nanoplatelets is presumably lower with chloride passivation than with carboxylate ligands.[62,63] This would decrease the barrier heights for growth on the side facets of nanoplatelets, inducing anisotropic (lateral) growth over a larger range of thicknesses. A similar reduction in the surface energy has been reported for {111} facets, which are relevant for MSNCs. Co-passivation with halide and amines lowers the surface energy compared to passivation with carboxylates.[57]

Motivated by the results for nanoplatelets, we exploited our model to test the effect of reduced surface energy on the growth kinetics of MSNCs. Figure 5a plots the energy barrier connecting two subsequent MSNC species as a function of MSNC size for two different surface energies (ε_A = 115 and 128 meV). For each species n, we compute the barriers at the corresponding 2D critical supersaturation, $\Delta\mu_{n+1,\mathrm{crit}}^{\mathrm{2D}}$. The lower value for ε_A, 115 meV, was chosen such that the ratio (0.89) of surface energies for carboxylate- and chloride-passivated surfaces was the same for our {111} facets as it was for {100} facets.[49,62] The results show that the barriers increase as the MSNC size increases, in line with the logarithmic time scale observed in Figure 4e. Further, they show that the lower surface energy decreases the barriers, independent of MSNC size. This should lead to faster dynamics and larger MSNCs.

To test this, we simulated MSNC growth with the same model as in Figure 4 but with reduced surface energy (ε_A = 115 meV). The initial monomer concentration, $\varepsilon_S/\varepsilon_A$ ratio, and reaction temperature were kept as in Figure 4. The results are plotted in Figure 5b as the monomer fraction for different MSNC species as a function of the normalized reaction time τ on a logarithmic scale. Vertical arrows compare when each MSNC species reached its maximum for ε_A = 128 meV (Figure 4e). Our simulations with reduced surface energy reveal that in the same time frame larger MSNC species appear. They suggest that by reducing the surface energy, *e.g.* by adding halides to the synthesis, the growth of MSNCs can be accelerated and extended to larger sizes.

Indeed, experiments confirm these predictions. We added cadmium chloride to our standard protocol for MSNCs at 180 °C. The growth was accelerated, as shown in Figure S13. Moreover, when we increased the temperature to 240 °C, we saw the continuation of discrete growth beyond 523. In particular, we could extend MSNCs to 554 (Figure S14). After isolating this species by size-selective precipitation, we measured its optical properties. Figure 5c,d shows its absorption, PLE, and PL spectra at room temperature. The latter displays a narrow emission peak at 567 nm [fwhm of 32.6 nm (126 meV)] with measured band-edge quantum yields as high as 65% (with typical values above 50%). When the particles were imaged using STEM (Figure 5e) we observed shapes with an average effective diameter (see Section S1.3 in the SI) of 3.3±0.4 nm. Moreover, because many of the particles had triangular profiles, which are consistent with tetrahedra in projection, these experimental results provide further support of the growth model presented above.

Our images also suggest that at least some of the tetrahedra have truncated vertices. If this is indeed the case, it is unclear if these additional exposed facets are present during the growth or appear during subsequent isolation or imaging. Assuming these exposed surfaces to be similar to the {111} facets considered in our model, we would expect the small facets on the truncated vertices to exhibit the

smallest barriers (and, hence, the fastest growth). This would argue for the formation of complete tetrahedra. However, further work is required both experimentally and theoretically to clarify the MSNC shape. In addition, the presence of some truncated vertices would imply that the imaged particles are not monodisperse. Thus, how uniform in size and shape such large MSNCs can be made remains an interesting open question.

CONCLUSIONS

We have presented a synthesis that produces magic-sized nanocrystals of CdSe up to a size of ~2.7 nm. The resulting species were isolated and investigated. Our analysis, in line with previous reports,[11,12,17,32] suggests that MSNCs correspond to tetrahedra of increasing size. Moreover, we have demonstrated that isolated MSNCs can be grown sequentially to the next-bigger size without Se precursor, molecular templates, or solvent. To explain these findings, we have proposed a microscopic model based on classical nucleation theory. We show that the combination of size-dependent nanoscale effects and the tetrahedral shape explain the existence of MSNCs and their sequential growth. Furthermore, our results imply that the growth of semiconductor MSNCs and nanoplatelets are closely related. Both depend on kinetic effects that arise at small size under surface-reaction-limited conditions. Based on insights from our model, we modified our synthetic protocol and extended the achievable size range of our MSNCs to ~3.3 nm. The obtained crystallites show tunable band-edge emission with high quantum yield at room temperature over a broad range of wavelengths. Thus, our work not only explains magic-sized growth, increasing fundamental knowledge about CdSe nanocrystals, but also produces larger MSNCs with superior optical properties. Finally, we believe that our findings are more general than the specific material system studied. They should allow other materials that exhibit "magic" behavior during growth[43,64] to be rationalized or targeted, moving toward a different strategy for nearly monodisperse nanocrystals than conventionally used to generate colloidal quantum dots.

ASSOCIATED CONTENT

Supporting Information

The Supporting Information is available below.

Experimental details for the synthesis, characterization, and size analysis of MSNCs, and descriptions of the nucleation-theory model and population-balance model, which describe MSNC stability and growth dynamics, respectively. (PDF)

AUTHOR INFORMATION

Corresponding Author

*Email: dnorris@ethz.ch.

Author Contributions

§A.S.M. and S.M. contributed equally to this work.

ORCID

Aniket Mule: 0000-0001-8387-080X

Sergio Mazzotti: 0000-0001-6314-9580

Aurelio A. Rossinelli: 0000-0001-6930-4190

Marianne Aellen: 0000-0003-1548-0433

P. Tim Prins: 0000-0002-8258-0074

Johanna C. van der Bok: 0000-0002-1810-3513

Simon F. Solari: 0000-0002-9874-1485

Yannik M. Glauser: 0000-0002-5362-0102

Priyank V. Kumar: 0000-0002-8203-7223

Andreas Riedinger: 0000-0002-7732-0606

David J. Norris: 0000-0002-3765-0678

Present Address

[▽]School of Chemical Engineering, University of New South Wales, Sydney 2052, Australia

Notes

The authors declare no competing financial interest.

ACKNOWLEDGMENTS

This work was primarily supported by the Swiss National Science Foundation (SNSF) under Award No. 200021-188593. A.A.R. acknowledges funding from SNSF Award No. 200021-165559. M.A. was supported by the European Research Council under the European Union's Seventh Framework Program (FP/2007-2013) / ERC Grant Agreement Nr. 339905 (QuaDoPS Advanced Grant). The authors thank F. Antolinez, K. Boldt, S. Handschin, R. Keitel, P. Knüsel, N. Lassaline, S. Meyer, F. Ott, A. Pun, H. Rojo, A. Sologubenko, G. Stemmler, and M. Wörle for technical assistance and discussions. This work benefitted from facilities at the Scientific Center for Optical and Electronic Microscopy (ScopeM) at ETH Zurich.

REFERENCES

(1) Klimov, V. I. *Nanocrystal Quantum Dots*, 2nd ed.; CRC Press: Boca Raton, 2010.

(2) Efros, A. L.; Efros, A. L. Interband Light Absorption in Semiconductor Spheres. *Sov. Phys. Semicond.* **1982**, *16*, 772–775.

(3) Brus, L. E. Electron-Electron and Electron-Hole Interactions in Small Semiconductor Crystallites: The Size Dependence of the Lowest Excited Electronic State. *J. Chem. Phys.* **1984**, *80*, 4403–4409.

(4) Murray, C. B.; Norris, D. J.; Bawendi, M. G. Synthesis and Characterization of Nearly Monodisperse CdE (E = Sulfur, Selenium, Tellurium) Semiconductor Nanocrystallites. *J. Am. Chem. Soc.* **1993**, *115*, 8706–8715.

(5) Peng, Z. A.; Peng, X. Formation of High-Quality CdTe, CdSe, and CdS Nanocrystals Using CdO as Precursor. *J. Am. Chem. Soc.* **2001**, *123*, 183–184.

(6) Peng, X.; Manna, L.; Yang, W.; Wickham, J.; Scher, E.; Kadavanich, A.; Alivisatos, A. P. Shape Control of CdSe Nanocrystals. *Nature* **2000**, *404*, 59–61.

(7) Ithurria, S.; Dubertret, B. Quasi 2D Colloidal CdSe Platelets with Thicknesses Controlled at the Atomic Level. *J. Am. Chem. Soc.* **2008**, *130*, 16504–16505.

(8) Ithurria, S.; Tessier, M. D.; Mahler, B.; Lobo, R. P. S. M.; Dubertret, B.; Efros, A. L. Colloidal Nanoplatelets with Two-Dimensional Electronic Structure. *Nat. Mater.* **2011**, *10*, 936–941.

(9) Hens, Z.; De Roo, J. Atomically Precise Nanocrystals. *J. Am. Chem. Soc.* **2020**, *142*, 15627–15637.

(10) Bootharaju, M. S.; Baek, W.; Lee, S.; Chang, H.; Kim, J.; Hyeon, T. Magic-Sized Stoichiometric II–VI Nanoclusters. *Small* **2020**, No. 2002067 (published online).

(11) Dance, I. G.; Choy, A.; Scudder, M. L. Syntheses, Properties, and Molecular and Crystal Structures of $(Me_4N)_4[E_4M_{10}(SPh)_{16}]$ (E = Sulfur or Selenium; M = Zinc or Cadmium): Molecular Supertetrahedral Fragments of the Cubic Metal Chalcogenide. *J. Am. Chem. Soc.* **1984**, *106*, 6285–6295.

(12) Lee, G. S. H.; Craig, D. C.; Ma, I.; Scudder, M. L.; Bailey, T. D.; Dance, I. G. $[S_4Cd_{17}(SPh)_{28}]^{2-}$, the First Member of a Third Series of Tetrahedral $[S_wM_x(SR)_y]^{Z-}$ Clusters. *J. Am. Chem. Soc.* **1988**, *110*, 4863–4864.

(13) Herron, N.; Calabrese, J. C.; Farneth, W. E.; Wang, Y. Crystal Structure and Optical Properties of $Cd_{32}S_{14}(SC_6H_5)_{36}$. DMF_4, a Cluster with a 15 Angstrom CdS Core. *Science* **1993**, *259*, 1426–1428.

(14) Karel Čapek, R.; Moreels, I.; Lambert, K.; De Muynck, D.; Zhao, Q.; Van Tomme, A.; Vanhaecke, F.; Hens, Z. Optical Properties of Zincblende Cadmium Selenide Quantum Dots. *J. Phys. Chem. C* **2010**, *114*, 6371–6376.

(15) Harrell, S. M.; Mcbride, J. R.; Rosenthal, S. J. Synthesis of Ultrasmall and Magic-Sized CdSe Nanocrystals. *Chem. Mater.* **2013**, *25*, 1199–1210.

(16) Kasuya, A.; Sivamohan, R.; Barnakov, Y. A.; Dmitruk, I. M.; Nirasawa, T.; Romanyuk, V. R.; Kumar, V.; Mamykin, S. V.; Tohji, K.; Jeyadevan, B.; Shinoda, K.; Kudo, T.; Terasaki, O.; Liu, Z.; Belosludov, R. V.; Sundararajan, V.; Kawazoe, Y. Ultra-Stable Nanoparticles of CdSe Revealed from Mass Spectrometry. *Nat. Mater.* **2004**, *3*, 99–102.

(17) Kudera, S. Formation of Colloidal Semiconductor Nanocrystals: The Aspect of Nucleation, Ph. D. Thesis, Ludwig-Maximilians-Universität München, Munich, October 2007.

(18) Williamson, C. B.; Nevers, D. R.; Nelson, A.; Hadar, I.; Banin, U.; Hanrath, T.; Robinson, R. D. Chemically Reversible Isomerization of Inorganic Clusters. *Science* **2019**, *363*, 731–735.

(19) Gary, D. C.; Flowers, S. E.; Kaminsky, W.; Petrone, A.; Li, X.; Cossairt, B. M. Single-Crystal and Electronic Structure of a 1.3 nm Indium Phosphide Nanocluster. *J. Am. Chem. Soc.* **2016**, *138*, 1510–1513.

(20) Cossairt, B. M.; Owen, J. S. CdSe Clusters: At the Interface of Small Molecules and Quantum Dots. *Chem. Mater.* **2011**, *23*, 3114–3119.

(21) Herron, N.; Suna, A.; Wang, Y. Synthesis of ≈ 10 Å Thiophenolate-Capped CdS Clusters. Observation of a Sharp Absorption Peak. *J. Chem. Soc., Dalton Trans.* **1992**, No. 15, 2329–2335.

(22) Ptatschek, V.; Schmidt, T.; Lerch, M.; Müller, G.; Spanhel, L.; Emmerling, A.; Fricke, J.; Foitzik, A. H.; Langer, E. Quantized Aggregation Phenomena in II-VI-Semiconductor Colloids. *Ber. Bunsen-Ges. Phys. Chem.* **1998**, *102*, 85–95.

(23) Evans, C. M.; Love, A. M.; Weiss, E. A. Surfactant-Controlled Polymerization of Semiconductor Clusters to Quantum Dots through Competing Step-Growth and Living Chain-Growth Mechanisms. *J. Am. Chem. Soc.* **2012**, *134*, 17298–17305.

(24) Wang, Y.; Liu, Y.-H.; Zhang, Y.; Wang, F.; Kowalski, P. J.; Rohrs, H. W.; Loomis, R. A.; Gross, M. L.; Buhro, W. E. Isolation of the Magic-Size CdSe Nanoclusters $[(CdSe)_{13}(n\text{-Octylamine})_{13}]$ and $[(CdSe)_{13}(Oleylamine)_{13}]$. *Angew. Chemie Int. Ed.* **2012**, *51*, 6154–6157.

(25) Wang, Y.; Zhou, Y.; Zhang, Y.; Buhro, W. E. Magic-Size II–VI Nanoclusters as Synthons for Flat Colloidal Nanocrystals. *Inorg. Chem.* **2015**, *54*, 1165–1177.

(26) Nevers, D. R.; Williamson, C. B.; Savitzky, B. H.; Hadar, I.; Banin, U.; Kourkoutis, L. F.; Hanrath, T.; Robinson, R. D.; Smith, R. F. Mesophase Formation Stabilizes High-Purity Magic-Sized Clusters. *J. Am. Chem. Soc.* **2018**, *140*, 3652–3662.

(27) Kudera, S.; Zanella, M.; Giannini, C.; Rizzo, A.; Li, Y.; Gigli, G.; Cingolani, R.; Ciccarella, G.; Spahl, W.; Parak, W. J.; Manna, L. Sequential Growth of Magic-Size CdSe Nanocrystals. *Adv. Mater.* **2007**, *19*, 548–552.

(28) Nguyen, K. A.; Pachter, R.; Jiang, J.; Day, P. N. Systematic Study of Structure, Stability, and Electronic Absorption of Tetrahedral CdSe Clusters with Carboxylate and Amine Ligands. *J. Phys. Chem. A* **2018**, *122*, 6704–6712.

(29) Voznyy, O.; Mokkath, J. H.; Jain, A.; Sargent, E. H.; Schwingenschlögl, U. Computational Study of Magic-Size CdSe Clusters with Complementary Passivation by Carboxylic and Amine Ligands. *J. Phys. Chem. C* **2016**, *120*, 10015–10019.

(30) Fojtik, A.; Weller, H.; Koch, U.; Henglein, A. Photo-Chemistry of Colloidal Metal Sulfides 8. Photo-Physics of Extremely Small CdS Particles: Q-State CdS and Magic Agglomeration Numbers. *Ber. Bunsen-Ges. Phys. Chem.* **1984**, *88*, 969–977.

(31) Dukes III, A. D.; Mcbride, J. R.; Rosenthal, S. J.; Dukes, A. D.; Mcbride, J. R.; Rosenthal, S. J. Synthesis of Magic-Sized CdSe and CdTe Nanocrystals with Diisooctylphosphinic Acid. *Chem. Mater.* **2010**, *22*, 6402–6408.

(32) Beecher, A. N.; Yang, X.; Palmer, J. H.; Lagrassa, A. L.; Juhas, P.; Billinge, S. J. L.; Owen, J. S. Atomic Structures and Gram Scale Synthesis of Three Tetrahedral Quantum Dots. *J. Am. Chem. Soc.* **2014**, *136*, 10645–10653.

(33) Yu, K. CdSe Magic-Sized Nuclei, Magic-Sized Nanoclusters and Regular Nanocrystals: Monomer Effects on Nucleation and Growth. *Adv. Mater.* **2012**, *24*, 1123–1132.

(34) Newton, J. C.; Ramasamy, K.; Mandal, M.; Joshi, G. K.; Kumbhar, A.; Sardar, R. Low-Temperature Synthesis of Magic-Sized CdSe Nanoclusters: Influence of Ligands on Nanocluster Growth and Photophysical Properties. *J. Phys. Chem. C* **2012**, *116*, 4380–4389.

(35) Wurmbrand, D.; Fischer, J. W. A.; Rosenberg, R.; Boldt, K. Morphogenesis of Anisotropic Nanoparticles: Self-Templating via Non-Classical, Fibrillar Cd_2Se Intermediates. *Chem. Commun.* **2018**, *54*, 7358–7361.

(36) Hudson, M. H.; Dolzhnikov, D. S.; Filatov, A. S.; Janke, E. M.; Jang, J.; Lee, B.; Sun, C.; Talapin, D. V. New Forms of CdSe: Molecular Wires, Gels, and Ordered Mesoporous Assemblies. *J. Am. Chem. Soc.* **2017**, *139*, 3368–3377.

(37) Bowers II, M. J.; McBride, J. R.; Rosenthal, S. J. White-Light Emission from Magic-Sized Cadmium Selenide Nanocrystals. *J. Am. Chem. Soc.* **2005**, *127*, 15378–15379.

(38) Ramsden, J. J.; Grätzel, M. Photoluminescence of Small Cadmium Sulphide Particles. *J. Chem. Soc., Faraday Trans. 1* **1984**, *80*, 919–933.

(39) Bawendi, M. G.; Wilson, W. L.; Rothberg, L.; Carroll, P. J.; Jedju, T. M.; Steigerwald, M. L.; Brus, L. E. Electronic Structure and Photoexcited-Carrier Dynamics in Nanometer-Size CdSe Clusters. *Phys. Rev. Lett.* **1990**, *65*, 1623–1626.

(40) Norris, D. J.; Bawendi, M. G. Measurement and Assignment of the Size-Dependent Optical Spectrum in CdSe Quantum Dots. *Phys. Rev. B* **1996**, *53*, 16338–16346.

(41) Joo, J.; Son, J. S.; Kwon, S. G.; Yu, J. H.; Hyeon, T. Low-Temperature Solution-Phase Synthesis of Quantum Well Structured CdSe Nanoribbons. *J. Am. Chem. Soc.* **2006**, *128*, 5632–5633.

(42) Hsieh, T.-E.; Yang, T.-W.; Hsieh, C.-Y.; Huang, S.-J.; Yeh, Y.-Q.; Chen, C.-H.; Li, E. Y.; Liu, Y.-H. Unraveling the Structure of Magic-Size $(CdSe)_{13}$ Cluster Pairs. *Chem. Mater.* **2018**, *30*,

5468–5477.

(43) Evans, C. M.; Guo, L.; Peterson, J. J.; Maccagnano-Zacher, S.; Krauss, T. D. Ultrabright PbSe Magic-Sized Clusters. *Nano Lett.* **2008**, *8*, 2896–2899.

(44) Evans, C. M.; Evans, M. E.; Krauss, T. D. Mysteries of TOPSe Revealed: Insights into Quantum Dot Nucleation. *J. Am. Chem. Soc.* **2010**, *132*, 10973–10975.

(45) Riedinger, A.; Mule, A. S.; Knüsel, P. N.; Ott, F. D.; Rossinelli, A. A.; Norris, D. J. Identifying Reactive Organo-Selenium Precursors in the Synthesis of CdSe Nanoplatelets. *Chem. Commun.* **2018**, *54*, 11789–11792.

(46) Knüsel, P. N.; Riedinger, A.; Rossinelli, A. A.; Ott, F. D.; Mule, A. S.; Norris, D. J. Experimental Evidence for Two-Dimensional Ostwald Ripening in Semiconductor Nanoplatelets. *Chem. Mater.* **2020**, *32*, 3312–3319.

(47) Abécassis, B.; Bouet, C.; Garnero, C.; Constantin, D.; Lequeux, N.; Ithurria, S.; Dubertret, B.; Pauw, B. R.; Pontoni, D. Real-Time in Situ Probing of High-Temperature Quantum Dots Solution Synthesis. *Nano Lett.* **2015**, *15*, 2620–2626.

(48) Castro, N.; Bouet, C.; Ithurria, S.; Lequeux, N.; Constantin, D.; Levitz, P.; Pontoni, D.; Abécassis, B. Insights into the Formation Mechanism of CdSe Nanoplatelets Using in Situ X-Ray Scattering. *Nano Lett.* **2019**, *19*, 6466–6474.

(49) Riedinger, A.; Ott, F. D.; Mule, A.; Mazzotti, S.; Knüsel, P. N.; Kress, S. J. P.; Prins, F.; Erwin, S. C.; Norris, D. J. An Intrinsic Growth Instability in Isotropic Materials Leads to Quasi-Two-Dimensional Nanoplatelets. *Nat. Mater.* **2017**, *16*, 743–748.

(50) Dhaene, E.; Billet, J.; Bennett, E.; Van Driessche, I.; De Roo, J. The Trouble with ODE: Polymerization during Nanocrystal Synthesis. *Nano Lett.* **2019**, *19*, 7411–7417.

(51) Ott, F. D.; Riedinger, A.; Ochsenbein, D. R.; Knuesel, P. N.; Erwin, S. C.; Mazzotti, M.; Norris, D. J. Ripening of Semiconductor Nanoplatelets. *Nano Lett.* **2017**, *17*, 6870–6877.

(52) Jiang, Y.; Ojo, W.-S.; Mahler, B.; Xu, X.; Abécassis, B.; Dubertret, B. Synthesis of CdSe Nanoplatelets without Short-Chain Ligands: Implication for Their Growth Mechanisms. *ACS Omega* **2018**, *3*, 6199–6205.

(53) Rossinelli, A. A.; Riedinger, A.; Marqués-Gallego, P.; Knüsel, P. N.; Antolinez, F. V.; Norris, D. J. High-Temperature Growth of Thick-Shell CdSe/CdS Core/Shell Nanoplatelets. *Chem. Commun.* **2017**, *53*, 9938–9941.

(54) Fritzinger, B.; Capek, R. K.; Lambert, K.; Martins, J. C.; Hens, Z. Utilizing Self-Exchange to Address the Binding of Carboxylic Acid Ligands to CdSe Quantum Dots. *J. Am. Chem. Soc.* **2010**, *132*, 10195–10201.

(55) Anderson, N. C.; Hendricks, M. P.; Choi, J. J.; Owen, J. S. Ligand Exchange and the Stoichiometry of Metal Chalcogenide Nanocrystals: Spectroscopic Observation of Facile Metal-Carboxylate Displacement and Binding. *J. Am. Chem. Soc.* **2013**, *135*, 18536–18548.

(56) Markov, I. V. *Crystal Growth for Beginners: Fundamentals of Nucleation, Crystal Growth and Epitaxy*, 2nd ed.; World Scientific: Singapore, 2017.

(57) Ko, J. H.; Yoo, D.; Kim, Y. H. Atomic Models for Anionic Ligand Passivation of Cation-Rich Surfaces of IV-VI, II-VI, and III-V Colloidal Quantum Dots. *Chem. Commun.* **2017**, *53*, 388–391.

(58) Reiss, H. The Growth of Uniform Colloidal Dispersions. *J. Chem. Phys.* **1951**, *19*, 482–487.

(59) Peng, X.; Wickham, J.; Alivisatos, A. P. Kinetics of II-VI and III-V Colloidal Semiconductor Nanocrystal Growth: "Focusing" of Size Distributions. *J. Am. Chem. Soc.* **1998**, *120*, 5343–5344.

(60) Cho, W.; Kim, S.; Coropceanu, I.; Srivastava, V.; Diroll, B. T.; Hazarika, A.; Fedin, I.; Galli, G.; Schaller, R. D.; Talapin, D. V. Direct Synthesis of Six-Monolayer (1.9 nm) Thick Zinc-Blende CdSe Nanoplatelets Emitting at 585 nm. *Chem. Mater.* **2018**, *30*, 6957–6960.

(61) Christodoulou, S.; Climente, J. I.; Planelles, J.; Brescia, R.; Prato, M.; Martín-García, B.; Khan, A. H.; Moreels, I. Chloride-Induced Thickness Control in CdSe Nanoplatelets. *Nano Lett.* **2018**, *18*, 6248–6254.

(62) Meerbach, C.; Wu, C.; Erwin, S. C.; Dang, Z.; Prudnikau, A.; Lesnyak, V. Halide-Assisted Synthesis of Cadmium Chalcogenide Nanoplatelets. *Chem. Mater.* **2020**, *32*, 566–574.

(63) Zherebetskyy, D.; Scheele, M.; Zhang, Y.; Bronstein, N.; Thompson, C.; Britt, D.; Salmeron, M.; Alivisatos, P.; Wang, L. W. Hydroxylation of the Surface of PbS Nanocrystals Passivated with Oleic Acid. *Science* **2014**, *344*, 1380–1384.

(64) Zanella, M.; Abbasi, A. Z.; Schaper, A. K.; Parak, W. J. Discontinuous Growth of II−VI Semiconductor Nanocrystals from Different Materials. *J. Phys. Chem. C* **2010**, *114*, 6205–6215.

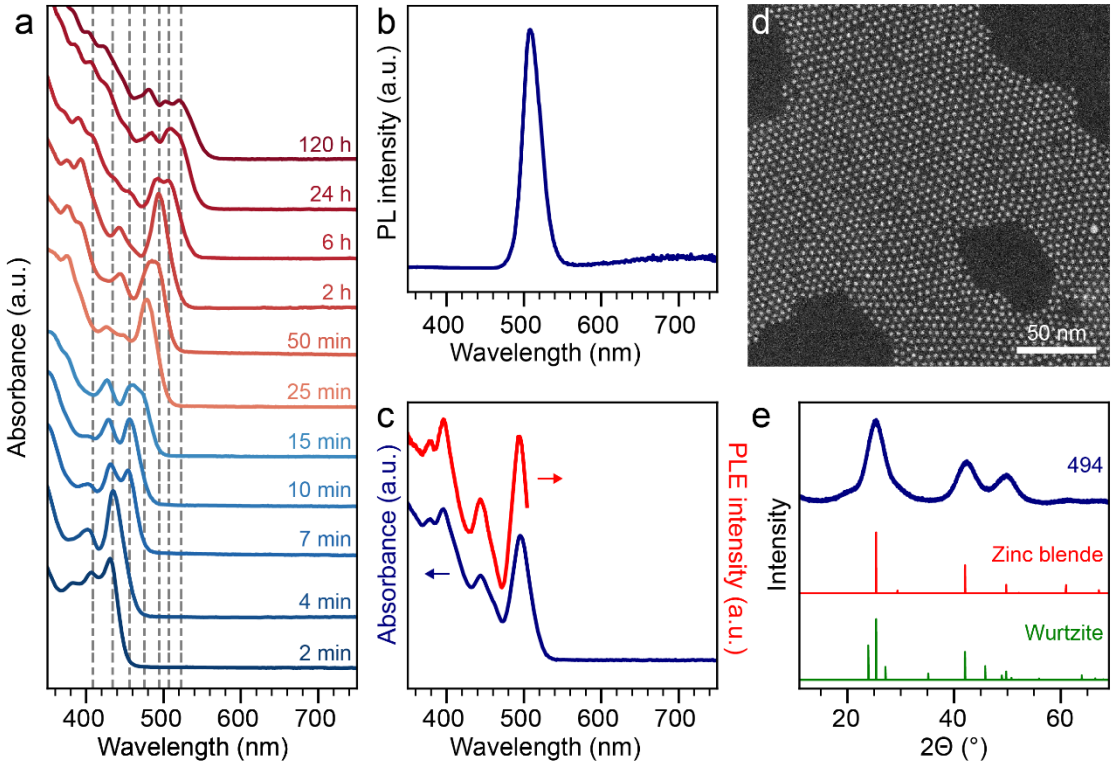

Figure 1. Optical and structural characterization of CdSe magic-sized nanocrystals (MSNCs). (a) Temporal evolution of the optical absorption spectra of CdSe MSNCs grown at 240 °C. Each spectrum is labelled with the time after injection. The vertical dashed lines indicate the lowest energy excitonic peaks for 7 MSNC product species (at 408, 434, 455, 476, 494, 508, and 523 nm). (b) Room-temperature photoluminescence (PL) spectrum of the isolated 494 species showing strong band-edge and weak trap emission. The excitation is at 300 nm. (c) Room-temperature photoluminescence excitation (PLE, red) and absorption (blue) spectra of the isolated 494 species. For PLE, the emission is monitored at 508 nm. (d) High-angle annular dark-field (HAADF) scanning transmission electron microscopy (STEM) image of the 494 species. No sign of molecular templates is observed. (e) Powder X-ray diffraction (XRD) pattern for 494 (blue). The patterns of zinc blende [red, powder diffraction file (PDF) 19-191] and wurtzite (green, PDF 8-459) for bulk CdSe are shown for reference.

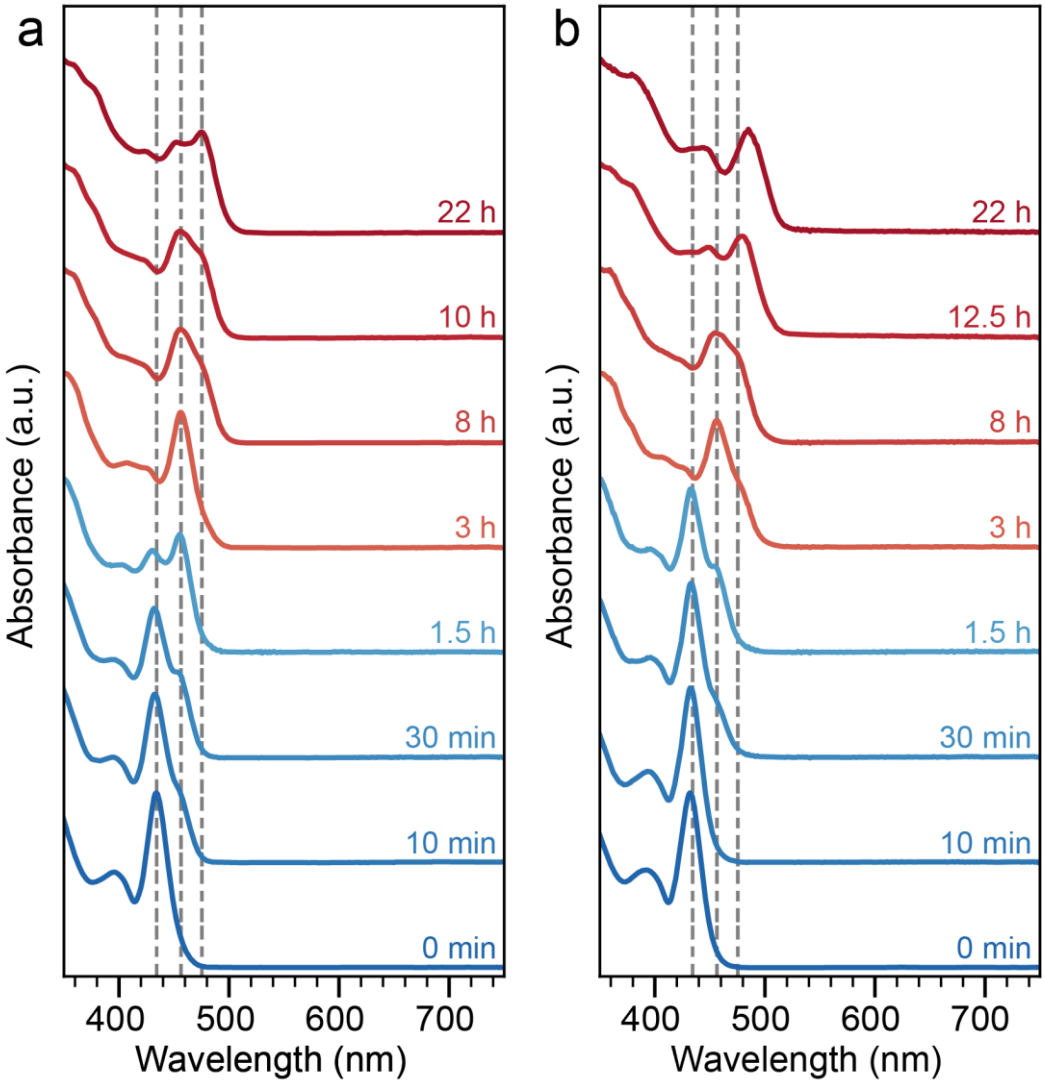

Figure 2. Growth of isolated CdSe MSNCs (434) without selenium precursor. (a) Temporal evolution of the optical absorption spectra of the isolated 434 species heated with cadmium myristate in 1-octadecene at 180 °C. Each spectrum is labelled with the growth time. The 434 species evolves to 455 and then 476. The vertical dashed lines are placed at 434, 455, and 476 nm. (b) Same as panel a, except without solvent. At 22 h, the sample has grown beyond 476.

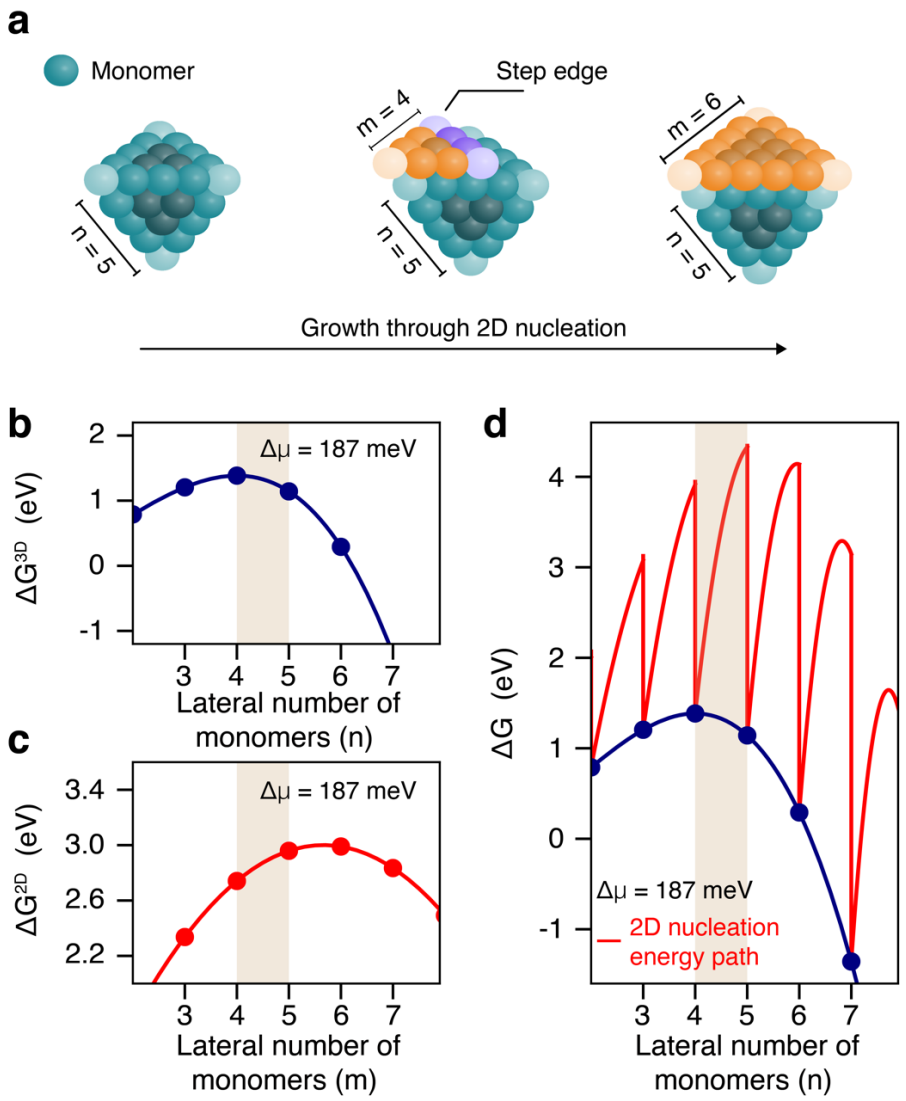

Figure 3. Growth of MSNCs by nucleation and lateral extension of 2D islands under constant supersaturation ($\Delta\mu$ = 187 meV). (a) Growth of tetrahedral-shaped MSNCs occurs through nucleation of a 2D island on one of the four identical facets. Monomers located at the step edge (purple) are energetically less favored compared to monomers on other edges of the MSNC due to the limited capability of ligands to passivate them. (b,c) Free energy associated with forming a 3D tetrahedron (ΔG^{3D}) and a 2D island (ΔG^{2D}), respectively. See text for details. (d) Combination of the 3D and 2D terms to describe the overall free energy of different sizes of MSNCs (blue dots) and the transition states (red lines) that link them. Results show that MSNCs correspond to local minima in the free energy with transition states between them that are thermodynamically unfavorable. Further, they show the existence of a size range where stable MSNCs are connected by size-dependent barriers (highlighted in beige).

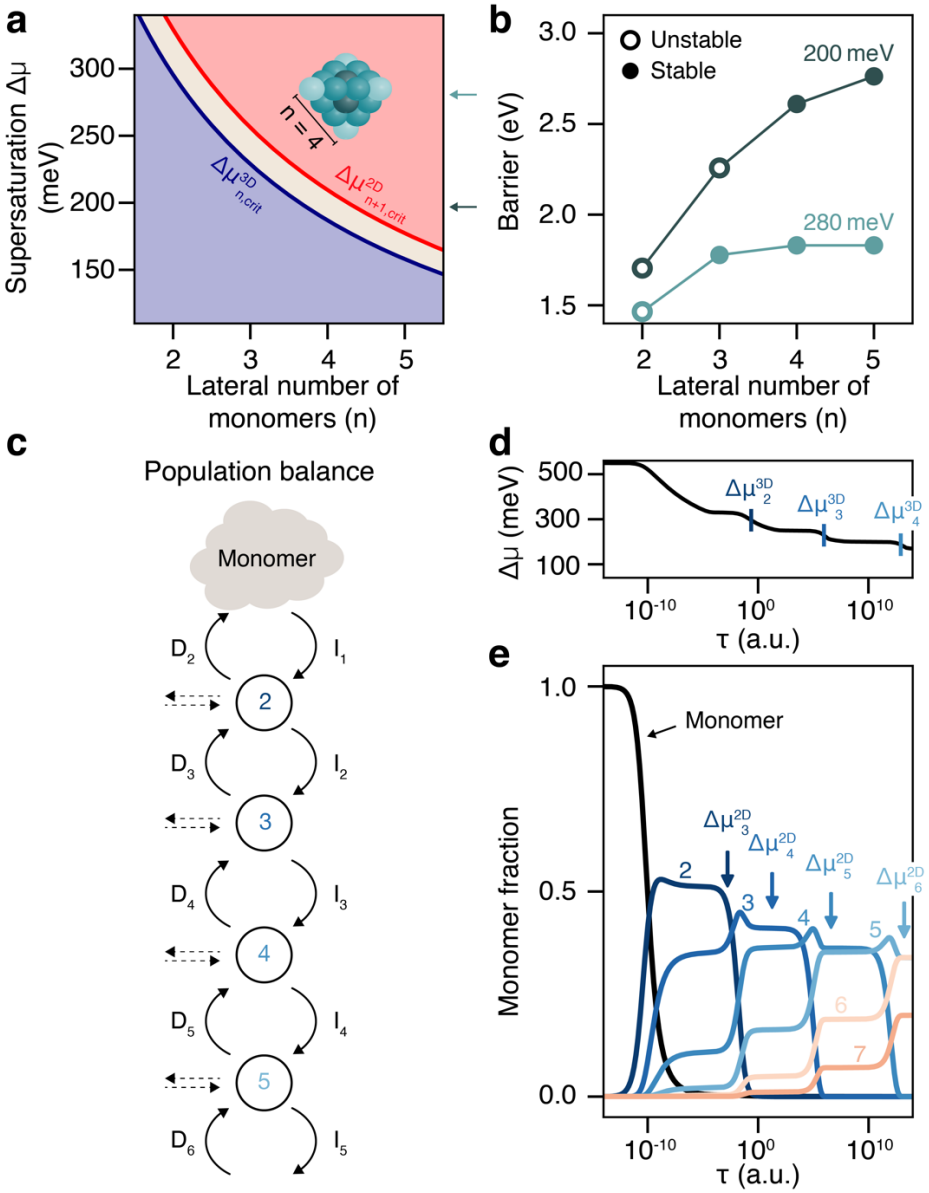

Figure 4. Population-balance model of MSNC growth. (a) Stability diagram displaying supersaturation ($\Delta\mu$) *versus* MSNC size. The red and blue curves display the 2D and 3D critical supersaturations, $\Delta\mu^{2D}_{n+1,crit}$ and $\Delta\mu^{3D}_{n,crit}$, respectively. Considering a horizontal slice through the stability diagram (*i.e.* at fixed supersaturation), the beige region delimits the size range of stable MSNCs exhibiting size-dependent barriers. (b) Barriers to transition from one size to the next are plotted for different sizes of MSNCs and for two different supersaturations (200 and 280 meV, highlighted with horizontal arrows in panel a). Decreasing $\Delta\mu$ shifts the size range of stable MSNCs exhibiting size-dependent barriers to larger sizes. (c) Sketch of the population-balance model displaying MSNC sizes and rates, I_n and D_n, connecting them. While only the smallest size (n = 2) is assumed to form directly from the monomer solution, growth and dissolution of larger MSNCs, dashed arrows, consume and generate monomers, respectively. (d) $\Delta\mu$ *versus* normalized reaction time τ. Vertical lines display time points at which $\Delta\mu$ equals the 3D critical supersaturation, $\Delta\mu^{3D}_{n,crit}$, of MSNC populations n = 2, 3, and 4. (d) Temporal evolution of different populations in terms of monomer fraction. Vertical arrows highlight time points at which $\Delta\mu$ equals the 2D critical supersaturation, $\Delta\mu^{2D}_{n+1,crit}$.

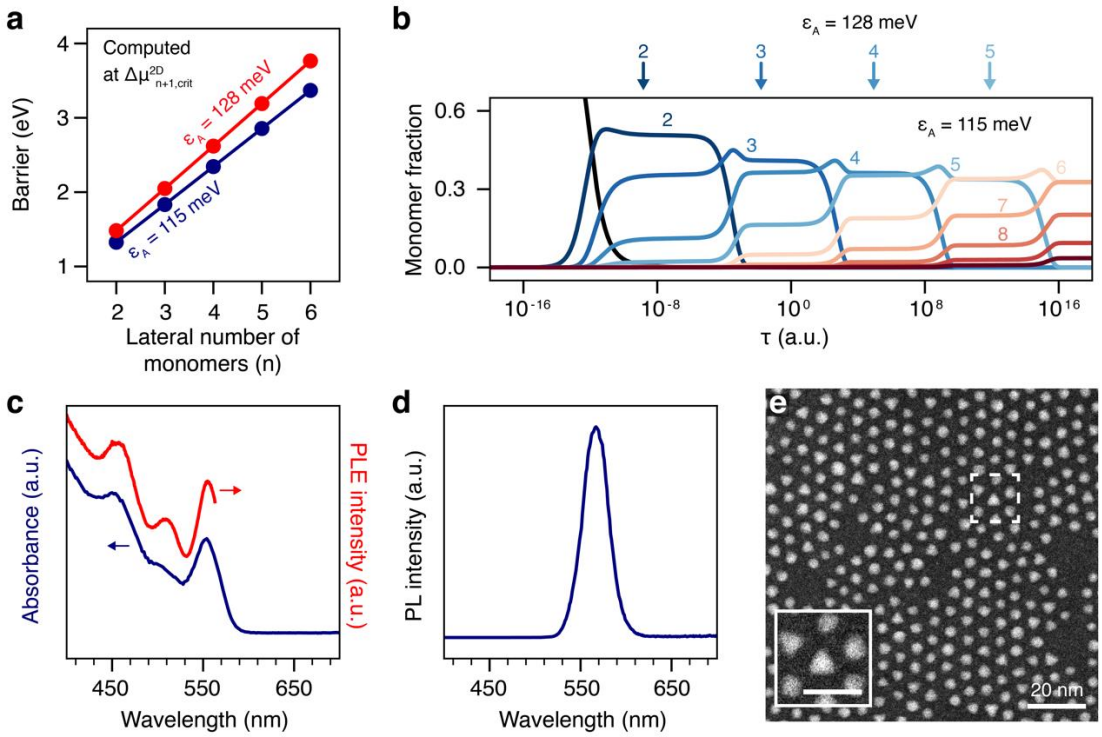

Figure 5. Extending CdSe MSNCs to larger sizes through addition of cadmium chloride. (a) Calculated barriers connecting different MSNC sizes plotted for two different surface energies, ε_A, of 115 and 128 meV. For each MSNC size, n, barriers are computed at the corresponding 2D critical supersaturation, $\Delta\mu^{2\mathrm{D}}_{n+1,\mathrm{crit}}$. See text for details. (b) Simulated temporal evolution of different MSNC sizes plotted in terms of monomer fraction. Results obtained for ε_A = 115 meV are displayed in the plot. For comparison, vertical arrows mark the maximum in monomer fraction for each MSNC size when ε_A = 128 meV is used. (c) Room-temperature photoluminescence excitation (PLE, red) and absorption (blue) spectra of the isolated 554 species synthesized by modifying the standard protocol by adding cadmium chloride. For PLE, the emission is monitored at 567 nm. (d) Room-temperature photoluminescence (PL) spectrum of the isolated 554 species. The excitation is at 300 nm. (e) HAADF STEM image of the 554 species. The inset shows the region in the white box magnified (with 10 nm scale bar). The electron micrographs of these bigger species reflect the tetrahedral shape reported previously for smaller MSNCs.

Supporting Information

Unraveling the Growth Mechanism of Magic-Sized Semiconductor Nanocrystals

Aniket S. Mule,[§,†] *Sergio Mazzotti,*[§,†] *Aurelio A. Rossinelli,*[†] *Marianne Aellen,*[†] *P. Tim Prins,*[‡] *Johanna C. van der Bok,*[‡] *Simon F. Solari,*[†] *Yannik M. Glauser,*[†] *Priyank V. Kumar,*[†,▽] *Andreas Riedinger,*[†,∥] *and David J. Norris*[*,†]

[†]Optical Materials Engineering Laboratory, Department of Mechanical and Process Engineering, ETH Zurich, 8092 Zurich, Switzerland

[‡]Condensed Matter and Interfaces, Debye Institute for Nanomaterials Science, Utrecht University, 3508 TA Utrecht, The Netherlands

[▽]Present Address: School of Chemical Engineering, University of New South Wales, Sydney 2052, Australia

[∥]Max-Planck-Institute for Polymer Research, Ackermannweg 10, 55128 Mainz, Germany

S1 EXPERIMENTAL DETAILS

S1.1 Synthetic methods of magic-sized nanocrystals (MSNCs)

Materials

Myristic acid (#70082, ≥98%), acetonitrile (#34998, ≥99.9%), trifluoroacetic acid (#302031, ≥99%), trifluoroacetic anhydride (#106232, ≥99%), selenium (Se, #209651, ≥99.5%), lithium aluminum hydride ($LiAlH_4$, #199877, 95%), toluene (#244511, 99.8%), diethyl ether (#676845, ≥98%), deuterated chloroform ($CDCl_3$, #236918, 99.6 atom % deuterium), 1-octadecene (ODE, #O806, 90%), oleic acid (#364525, 90%), cadmium acetate dihydrate (#289159, 98%), cadmium chloride (technical grade, #655198), and methyl acetate (≥98%, #W267600) were purchased from Sigma Aldrich. Triethyl amine (#157910010, 99%) and tetrahydrofuran (THF, #348450010, 99.5%) were purchased from Acros Organics. Cadmium oxide (#48-0800, 99.999%–Cd) was purchased from Strem Chemicals. Stearoyl chloride (#S0404, >97%) was purchased from TCI chemicals. Sodium chloride (NaCl, #85139.360) was purchased from VWR chemicals. Hexane, methanol, and 2-propanol were purchased from Thommen-Furler AG. Absolute ethanol was purchased from Alcosuisse AG. All chemicals were used as received. Deionized (DI) water was obtained from a Milli-Q Advantage A10 water purification system (Merck Millipore).

Synthesis of cadmium myristate

Cadmium myristate was synthesized by modifying the synthesis of lead oleate carried out by Hendricks *et al*.[S1] Briefly, 44.8 mmol (5.75 g) of cadmium (II) oxide was mixed with 20 mL of acetonitrile in a 100-mL three-neck round-bottomed flask. The mixture was stirred at 0 °C for 10 min. 8.96 mmol (0.7 mL, 0.2 equiv.) of trifluoroacetic acid and 44.8 mmol (6.2 mL, 1 equiv.) of trifluoroacetic anhydride are then added. After 15 min, the brownish mixture is heated to 50 °C to obtain a clear cadmium trifluoroacetate solution. In a separate 500-mL Erlenmeyer flask, 90.05 mmol of myristic acid (20.56 g, 2.01 equiv.), 101.25 mmol of triethyl amine (10.246 g, 2.26 equiv.) were added to 180 mL of 2-propanol. The cadmium trifluoroacetate solution was then gradually added to the myristic acid solution with stirring. The resulting white precipitate of cadmium myristate was isolated by suction filtration using a glass fritted funnel. The filtrate was thoroughly washed further 3 times with methanol (300 mL) and then dried under vacuum at room temperature for >12 h. The final product was grinded into fine powder and stored under ambient conditions.

Synthesis of bis(stearoyl) selenide

Synthesis of bis(stearoyl) selenide was carried out by adapting a protocol reported by Koketsu *et al.*[S2] Briefly, a suspension of elemental Se (1.92 g, 24 mmol) and dry THF (200 mL) was prepared in a 500-mL four-neck flask and kept at –10 °C (ice bath with NaCl) under N_2. $LiAlH_4$ (0.76 g, 20 mmol) was then added and the mixture was stirred to form LiAlHSeH. After 30 min, 20 mmol (6.8 mL) of stearoyl chloride was added over a span of 2 min to the solution of LiAlHSeH. This was repeated at 60, 90, and 120 min. The reaction was stopped after 150 min by adding 5 mL of DI water. The ice bath was removed and the reaction mixture was diluted by 250 mL of diethyl ether. The reaction mixture was further washed 4 times with 150 mL of a saturated NaCl solution. The turbid mixture was heated to ~50 °C to form a clear solution. The flask was left at room temperature for >10 h to induce crystallization of the desired product. The recrystallized product was separated by filtration and vacuum dried for >12 h at 25 °C. The product was stored in inert atmosphere (N_2) for further use. ^{1}H NMR ($CDCl_3$, 400 MHz): δ 0.88 (t, 6H, *J* = 6.8 Hz), 1.25 (s, 56H), 1.65 (quint, 4H, *J* = 7.5 Hz), 2.81 (t, 4H, *J* = 7.4 Hz). ^{13}C NMR ($CDCl_3$, 400 MHz): δ 14.28, 22.86, 24.96, 28.91, 29.39, 29.53, 29.86, 32.09, 49.70, 198.34. ^{77}Se NMR ($CDCl_3$, 400 MHz): δ 809.94.

Synthesis of MSNC 434

0.3 mmol (80 mg) of cadmium acetate dihydrate, 0.7 mmol (197.7 mg, 222 µL) of oleic acid, and 15 mL of ODE were mixed in a 50-mL three-neck flask. The mixture was heated to 110 °C and degassed under vacuum for 90 min. After degassing, the mixture was heated to 180 °C under N_2. Simultaneously, 0.15 mmol (92 mg) of bis(stearoyl) selenide was dissolved in 2 mL of toluene under N_2. Mild heating (~35 °C) may be employed to obtain complete dissolution. Once the cadmium oleate solution reached 180 °C, the solution of bis(stearoyl) selenide was rapidly injected into the hot mixture. The MSNCs

were allowed to grow at 180 °C. After 25 min, the mixture was rapidly cooled down to room temperature by placing the flask in a water bath. The reaction-mixture volume was increased to ~30 mL by adding 15 mL of hexane and 1 mL of oleic acid. 150 mL of methyl acetate was added, and the sample was centrifuged at 8586 g (8000 rpm) for 5 min. The precipitate was re-dispersed in 5 mL of hexane. The washing cycle was repeated once by adding 25 mL of methyl acetate, centrifuged, and the precipitate was dispersed in 5 mL of toluene. The final washing cycle was carried out by adding 2.5 mL of acetonitrile to the sample and carrying out the centrifugation at 8586 g (8000 rpm) for 5 min. The final product (precipitate) was stored in 5 mL of hexane.

Synthesis of MSNC 455

The synthesis of MSNC 455 was very similar to MSNC 434 except for the synthesis temperature, the duration, and the steps associated with the subsequent cleaning. Briefly, 0.3 mmol (80 mg) of cadmium acetate dihydrate, 0.7 mmol (197.7 mg, 222 μL) of oleic acid, and 15 mL of ODE were mixed in a 50-mL three-neck flask. The mixture was heated to 110 °C and degassed under vacuum for 90 min. After degassing, the mixture was heated to 210 °C under N_2. Simultaneously, 0.15 mmol (92 mg) of bis(stearoyl) selenide was dissolved in 2 mL of toluene under N_2. Mild heating (~35 °C) may be employed to obtain complete dissolution. Once the cadmium oleate solution reached 210 °C, the solution of bis(stearoyl) selenide was rapidly injected into the hot mixture. Note that the temperature drops to 190 °C on injection of the selenium precursor. The system needs to be manually purged to return the temperature to 210 °C in ~5 min. This manual purge was done by taking a 1-mL syringe and pulling out ~200 μL of gas from the reaction flask every minute for a total of 5 min. The reaction was stopped after 27 min and 30 s and the mixture was rapidly cooled to ~180 °C with an air gun and then with a water bath to room temperature. The reaction-mixture volume was increased to ~30 mL by adding 15 mL of hexane and 1 mL of oleic acid. Since the reaction mixture in this case often contains a significant proportion of undesired smaller MSNC sizes, special care must be taken to ensure efficient separation in the first step of precipitation. 3 mL of ethanol was added to the reaction mixture. ~100 mL of methyl acetate was then added in small quantities with continuous stirring until the solution turned turbid. As soon as this occurred, 6 mL of methyl acetate was added. The sample was centrifuged at 8586 g (8000 rpm) for 5 min and the precipitate containing the 455 species was re-dispersed in 5 mL of hexane. 1 mL of ethanol and 25 mL of methyl acetate was added, and the centrifugation was repeated at 8586 g (8000 rpm) for 5 min. The precipitate was re-dispersed in 5 mL of toluene. The final washing cycle was carried out by adding 2.5 mL of acetonitrile to the sample and centrifuging at 8586 g (8000 rpm) for 5 min. The final product (precipitate) was stored in 5 mL of hexane.

Synthesis of MSNC 476

The synthesis of MSNC 476 was very similar to MSNC 434 except for the synthesis temperature, the duration, and the steps associated with the subsequent cleaning. Briefly, 0.3 mmol (80 mg) of cadmium

acetate dihydrate, 0.7 mmol (197.7 mg, 222 µL) of oleic acid, and 15 mL of ODE were mixed in a 50-mL three-neck flask. The mixture was heated to 110 °C and degassed under vacuum for 90 min. After degassing, the mixture was heated to 210 °C under N_2. Simultaneously, 0.15 mmol (92 mg) of bis(stearoyl) selenide was dissolved in 2 mL of toluene under N_2. Mild heating (~35 °C) may be employed to obtain complete dissolution. Once the cadmium oleate solution reached 210 °C, the solution of bis(stearoyl) selenide was rapidly injected into the hot mixture. Note that the temperature drops to 190 °C on injection of the selenium precursor. The system needs to be manually purged to return the temperature to 210 °C in ~5 min. This manual purge was done by taking a 1-mL syringe and pulling out ~200 µL of gas from the reaction flask every minute for a total of 5 min. The reaction was stopped after 2 h and the mixture was rapidly cooled to ~180 °C with an air gun and then with a water bath to room temperature. The reaction-mixture volume was increased to ~30 mL by adding 15 mL of hexane and 1 mL of oleic acid. Subsequently, 5.5 mL of ethanol and 90 mL of methyl acetate were added to the reaction mixture. The sample was centrifuged at 8586 g (8000 rpm) for 5 min, and the precipitate was collected and re-dispersed in 15 mL of hexane. 2.5 mL of ethanol and 45 mL of methyl acetate were added and centrifugation was repeated at 8586 g (8000 rpm) for 5 min. The precipitate was re-dispersed in 6 mL of toluene, and 200 µL of oleic acid was added. The final washing cycle was carried out by adding 3 mL of acetonitrile to the sample and centrifuging at 8586 g (8000 rpm) for 5 min. The final product (precipitate) was stored in 5 mL of hexane.

Synthesis of MSNC 494

0.6 mmol (160 mg) of cadmium acetate dihydrate, 1.4 mmol (395.4 mg, 444 µL) of oleic acid, and 15 mL of ODE were mixed in a 50-mL three-neck flask. The mixture was heated to 110 °C and degassed under vacuum for 90 min. After degassing, the mixture was heated to 240 °C under N_2. Simultaneously, 0.15 mmol (92 mg) of bis(stearoyl) selenide was dissolved in 2 mL of toluene under N_2. Mild heating (~35 °C) may be employed to obtain complete dissolution. Once the cadmium oleate solution reached 240 °C, the solution of bis(stearoyl) selenide was rapidly injected into the hot mixture. Note that the temperature drops to 200 °C on injection of the selenium precursor. The system needs to be manually purged to return the temperature to 240 °C in ~10 min. This manual purge was done by taking a 1-mL syringe and pulling out ~200 µL of gas from the reaction flask every minute for a total of 10 min. The MSNCs were allowed to grow at 240 °C. The reaction was stopped after 90 min, and the mixture was rapidly cooled down to ~180 °C with an air gun and then with a water bath to room temperature. The reaction-mixture volume was increased to ~30 mL by adding 15 mL of hexane and 1 mL of oleic acid. Subsequently, 6 mL of ethanol and 75 mL of methyl acetate were added to the reaction mixture. The sample was centrifuged at 8586 g (8000 rpm) for 5 min, and the precipitate was re-dispersed in 15 mL of hexane. 3 mL of ethanol and 30 mL of methyl acetate were added and centrifugation was repeated at 8586 g (8000 rpm) for 5 min. The precipitate was re-dispersed in 6 mL of toluene and 200 µL of oleic acid was added. The final washing cycle was carried out by adding 2.5 mL of acetonitrile to the sample

and centrifuging it at 8586 g (8000 rpm) for 5 min. The final product (precipitate) was stored in 5 mL of hexane.

Note: While the MSNC products so far have been synthesized using cadmium oleate (formed *in situ*) as the cadmium source, they can also be prepared using cadmium carboxylates. The exact parameters might vary slightly depending on which long-chain cadmium carboxylate is used. Small variations in outcomes are also observed with different batches of bis(stearoyl) selenide. These changes can be corrected for by slightly increasing or decreasing the duration of the synthesis.

Synthesis of MSNC 554

1.31 mmol (744.4 mg) of cadmium myristate, 0.38 mmol (68.6 mg) of cadmium chloride, and 15 mL of ODE were mixed in a 50-mL three-neck flask. The mixture was heated to 110 °C and degassed under vacuum for 30 min. After degassing, the mixture was heated to 240 °C under N_2. Simultaneously, 0.15 mmol (92 mg) of bis(stearoyl) selenide was dissolved in 2 mL of toluene under N_2. Mild heating (~35 °C) may be employed to obtain complete dissolution. Once the cadmium precursor reached 240 °C, the solution of bis(stearoyl) selenide was rapidly injected into the hot mixture. Note that the temperature drops to 200 °C on injection of the selenium precursor. The system needs to be manually purged to return the temperature to 240 °C in ~10 min. This manual purge was done by taking a 1-mL syringe and pulling out ~200 μL of gas from the reaction flask every minute for a total of 10 min. The MSNCs were allowed to grow at 240 °C. The reaction was stopped after 4 h, and the mixture was cooled to ~110 °C with an air gun. 10 mL of toluene was then added and the mixture was allowed to return to room temperature. 5 mL of hexane was added and the mixture was centrifuged at 2147 g (4000 rpm) for 5 min. The precipitate was re-dispersed in a mixture of 10 mL of hexane and 1 mL of oleic acid by sonication for 5 min. The mixture was then centrifuged at 8586 g (8000 rpm) for 5 min. The supernatant was separated. Since the supernatant in this case often contains a significant proportion of undesired smaller sizes and larger crystallites, special care must be taken to ensure efficient separation. ~20 mL of methyl acetate was added in small quantities with continuous stirring to the supernatant until the solution became slightly turbid. It was then centrifuged at 8586 g (8000 rpm) for 5 min. The precipitate was discarded. The supernatant was retained, and ~4 mL of methyl acetate was added to it. This mixture was again centrifuged at 8586 g (8000 rpm) for 5 min. The supernatant was discarded, and the precipitate containing the 554 species was re-dispersed in 3 mL of hexane. 10 mL of methyl acetate was again added, and centrifugation was repeated at 8586 g (8000 rpm) for 5 min. The final product (precipitate) was stored in 2 mL of hexane.

S1.2 Growth of isolated MSNCs

MSNC 434 was synthesized as described above. The sample was diluted with hexane to have an optical density at the lowest energy excitonic transition (434 nm) equivalent to ~20 for a 1-cm path length.

With solvent and ligands

6 mL of MSNC 434 dispersion was mixed with excess methyl acetate (~25 mL) and centrifuged at 7547 g (7500 rpm) for 10 min. The precipitate was re-dispersed in ODE and transferred to a 3-neck round-bottomed flask. 68 mg of cadmium myristate was added and the mixture was degassed under vacuum at 110 °C. After 30 min, the system was flushed with N_2, and the temperature was raised to 180 °C to carry out the growth of the MSNCs. Aliquots were taken at regular intervals to monitor the growth using absorption spectroscopy.

With ligands only

10 vials were each filled with 0.5 mL of MSNC 434 dispersion. 2.5 mL of methyl acetate was then added to each vial. The mixtures were centrifuged to precipitate out the magic-sized nanocrystals. 6 mg of cadmium myristate was added to each vial, which were subsequently placed in a pre-heated muffle furnace at 180 °C under N_2. The growth was monitored by removing a vial at a series of time points. 1 mL of hexane and 100 μL of oleic acid were added to the cooled vials. They were sonicated for ~5 min to re-disperse the MSNCs for further analysis.

With solvent only

6 mL of MSNC 434 dispersion was mixed with excess methyl acetate (~25 mL) and centrifuged at 7547 g (7500 rpm) for 10 min. The precipitate was re-dispersed in ODE and transferred to a 3-neck round-bottomed flask. The dispersion was degassed under vacuum at 110 °C. After 30 min, the system was flushed with N_2, and the temperature was raised to 180 °C to carry out the growth of the MSNCs. Aliquots were taken at regular intervals to monitor the growth.

S1.3 Characterization methods

Absorption spectroscopy

MSNCs were characterized using a Varian Cary Scan 50 ultraviolet-visible (UV-vis) spectrophotometer. The wavelength range from 300-800 nm was analyzed. The aliquots were measured by diluting them in 2 mL of hexane, 100 μL of oleic acid, and 20 μL of ethanol (dilution factor of 20). The samples were measured using a 1-cm path-length quartz cuvette.

Photoluminescence (PL) and photoluminescence excitation (PLE) spectroscopy

The PL and PLE spectra were recorded at room temperature (~23 °C) using an Edinburgh Instruments FLS 980 photoluminescence spectrometer. The samples were measured using a 1-cm path-length quartz cuvette by diluting them in hexane to an optical density of 0.1 at the lowest energy exciton transition.

Photoluminescence quantum yield (PLQY)

PLQY was measured at room temperature using a Hamamatsu C11347 Quantaurus-QY spectrometer equipped with an integrating sphere. The excitation wavelength was 400 nm. Purified MSNC samples

were diluted in hexane and measured in quartz cuvettes with a 1-cm path length. The cuvettes were cleaned in a 1% solution of Hellmanex™ III after each sample to ensure accurate results.

Powder X-ray diffraction (XRD)

The XRD spectra were recorded on a Bruker D8 Advance instrument (40 kV, 40 mA, $\lambda_{CuK\alpha}$ = 0.15418 nm). The samples for XRD were prepared by drop-casting concentrated hexane dispersions of MSNCs onto zero-background Si sample holders.

Transmission electron microscopy (TEM)

Transmission electron microscopy (TEM) micrographs were recorded on a JEOL JEM-1400 Plus, operated at 120 kV, or an FEI Talos F200X, operated at 200 kV. The scanning transmission electron microscopy (STEM) micrographs were recorded at 200 kV on an FEI Talos F200X fitted with a high-angle annular dark-field (HAADF) detector. The samples were prepared by drop-casting hexane dispersions of MSNCs (optical density of ~0.6 at the lowest energy excitonic transition for a 1-cm path length) onto 6-nm-thick carbon films supported by 200-mesh copper grids. It is important to note that damage is induced by the electron beam (Figure S7). To minimize this, microscope alignment was carried out at a particular sample location. However, images were recorded rapidly just outside this location.

Size analysis

For the size analysis, raw 1024x1024 pixel HAADF-STEM images were evaluated. While high magnifications can give a more precise particle-size estimation, it comes at the cost of accuracy due to beam damage (Figure S7). In contrast, low magnifications and large spot sizes minimize beam damage and give more accurate measurements. However, pixel discretization of the detector ultimately limits the precision. For the electron microscope used, this was optimized by choosing a magnification of 450,000X. All particle batches were imaged under identical operating conditions to keep other unknown errors systematic. Nevertheless, uncontrollable parameters during the synthesis, sample preparation, and imaging cannot be completely avoided, introducing random errors that can potentially adversely affect both precision and accuracy of the particle-size estimation. To minimize bias, the images were analyzed with a custom Python script. First a bandpass filter was applied in the Fourier-transformed image to eliminate high-frequency noise and reduce intensity variations in the background (low-frequency noise). The minimum and maximum features for the bandpass filter were set to 1 and 12 nm, respectively. Then, 48 pixels were cropped from each edge, to exclude edge effects of the electron beam. A binary Otsu threshold was applied to separate the objects (here MSNCs) from the background. Detected objects that touch an image border or have an area that is smaller than 1 nm^2 were ignored for further analyses. The area was calculated by the number of pixels the object spanned. The effective diameters (d) were extracted by assuming the areas of the detected objects (A) to be equal to a circle of same area, *i.e.* $d = \sqrt{4A/\pi}$.

Nuclear magnetic resonance spectroscopy (NMR)

All spectra were collected on a Bruker Ascend Aeon 400-MHz spectrometer. ^{1}H-NMR, ^{13}C-NMR, and ^{77}Se-NMR spectra were recorded with predefined pulse programs. The samples for NMR were prepared by dispersing MSNCs in $CDCl_3$.

S2 NUCLEATION THEORY APPLIED TO MSNCs

S2.1 Geometric description of MSNC

XRD measurements of MSNCs reveal that they are crystalline with a zinc-blende lattice. In line with previous reports,[S3,S4] we assume that their shape is tetrahedral and the exposed nanocrystal facets are Cd-terminated {111} surfaces. Our model uses the geometric properties of tetrahedra to facilitate the description of MSNCs. The lateral number of monomers (n) (see Figure 3a in the main text) defines all geometric quantities needed in our model: the total number of monomers on an edge, on a surface facet, and in a MSNC. The number of monomers on an edge is n, the number of monomers on a MSNC facet is given by the triangular number [$\Gamma(n)$], and the total number of monomers in a MSNC is given by the tetrahedral number [$\Phi(n)$]. The tetrahedral and triangular number, together with related properties, are defined below:

$$\Phi(n) = \sum_{i=1}^{n} \Gamma(i) = \frac{n(n+1)(n+2)}{6};\ \frac{d\Phi}{dn} = \frac{3n^2+6n+2}{6}, \tag{S1}$$

$$\Gamma(n) = \sum_{i=1}^{n} i = \frac{n(n+1)}{2};\ \frac{d\Gamma}{dn} = \frac{2n+1}{2}, \tag{S2}$$

$$\Phi(n) = \Phi(n-1) + \Gamma(n)\ . \tag{S3}$$

The definition provided in eq S3 links the tetrahedral and triangular numbers. It has a straightforward physical interpretation: covering one of the four identical facets of a tetrahedron [lateral size $(n-1)$] with a triangular surface (lateral size n), yields the next-larger tetrahedron (lateral size n).

S2.2 Energy of forming 3D nuclei and 2D surface islands

As discussed in the main text, we describe the energy of forming a 3D nucleus using classical nucleation theory. For a tetrahedral-shaped 3D nucleus with *n* monomers on its side, the energy of formation is given as:

$$\Delta G^{3D}(n) = -\Phi(n)\Delta\mu + 4\varepsilon_A\Gamma(n)\ , \tag{S4}$$

where $\Delta\mu$ is the supersaturation, *i.e.* the difference in chemical potential between a monomer in the solution and in the bulk crystal. The energy of breaking a crystalline bond and passivating it with a ligand is described by ε_A. It relates to the surface energy (σ_A) as $\varepsilon_A = \sigma_A\rho_A$, where ρ_A is the surface area per dangling bond. Monomers located within the surface exhibit one dangling bond, while monomers at the edges or vertices of MSNCs exhibit two and three dangling bonds, respectively. Each monomer at these sites exhibits exactly one dangling bond per surface that includes them. Therefore,

$4\Gamma(n)$ is the total number of dangling bonds per MSNC of size n. For simplicity, we will refer to ε_A as the surface energy.

The energy of forming a 2D island growing on the surface of a MSNC is given as:

$$\Delta G^{2D}(m) = \begin{cases} -\Gamma(m)\Delta\mu + 4\varepsilon_A m + \varepsilon_S m & \text{if } m < n+1 \\ -\Gamma(m)\Delta\mu + 4\varepsilon_A m & \text{if } m = n+1 \end{cases}. \quad \text{(S5)}$$

Here, m is the lateral number of monomers forming the 2D surface island (see Figure 3a in the main text). The step energy, ε_S, accounts for the fact that ligand passivation at the step front is different, compared to other surface sites. When the facet of a MSNC is completed, we need to account for the disappearance of the step front. For an MSNC of size n, this occurs when a 2D surface island of size $m = n + 1$ is formed.

S2.3 Effects of changes in supersaturation

In the main text, the stability of different-sized MSNCs as well as the transition states that link them, is plotted for fixed supersaturation (see Figure 3d in the main text). However, as nucleation and growth proceed, the monomer concentration in the melt decreases, thus decreasing the supersaturation. Here, we aim to provide a detailed derivation of how changes in supersaturation affect nucleation and growth. In Figure S11 we plot the overall energy-of-formation curve for forming MSNCs at different supersaturations. As the supersaturation decreases, energy barriers linking different-sized MSNCs increase. Further, the critical size for forming a 3D nucleus increases. This means that the threshold size for MSNC stability increases. Finally, the size range of MSNCs exhibiting size-dependent barriers shifts to larger sizes.

We wish to establish the link between the critical size of forming a 3D nucleus (n_{crit}^{3D}) and the critical supersaturation [$\Delta\mu_{\text{crit}}^{3D}(n)$] at which a 3D nucleus of lateral size n dissolves. The critical size of forming a 3D nucleus (n_{crit}^{3D}) is defined as:

$$\left.\frac{\partial \Delta G^{3D}}{\partial n}\right|_{n_{\text{crit}}^{3D}} = \left[-\left(\frac{3n^2+6n+2}{6}\right)\Delta\mu + 4\varepsilon_A\left(\frac{2n+1}{2}\right)\right]\Big|_{n_{\text{crit}}^{3D}} = 0\,. \quad \text{(S6)}$$

Eq S6 describes how the 3D critical size (n_{crit}^{3D}) depends on supersaturation or, *vice versa*, it defines the critical supersaturation [$\Delta\mu_{n,\text{crit}}^{3D}$] below which a MSNC of given size (n) dissolves:

$$\Delta\mu_{n,\text{crit}}^{3D} = \frac{12\varepsilon_A(2n+1)}{3n^2+6n+2}\,. \quad \text{(S7)}$$

From eq S7 we recognize that larger MSNCs exhibit a smaller 3D critical supersaturation. In turn, as the supersaturation decreases, n_{crit}^{3D} increases.

We follow a similar procedure to determine how the size range of MSNCs that exhibit size-dependent barriers varies with supersaturation. At fixed supersaturation, the energy of growing on a bulk facet is

linked to a 2D island with a lateral number of monomers, $m_{\mathrm{crit}}^{2\mathrm{D}}$. Because $m_{\mathrm{crit}}^{2\mathrm{D}}$ determines the growth barrier on a bulk facet [$\Delta G^{2\mathrm{D}}(m_{\mathrm{crit}}^{2\mathrm{D}})$], the barriers involved in growing 2D islands with a lateral number of monomers larger or equal to $m_{\mathrm{crit}}^{2\mathrm{D}}$ are identical to that of the bulk, *i.e.* size independent. In contrast, the barriers for growing 2D islands with a lateral number of monomers smaller than $m_{\mathrm{crit}}^{2\mathrm{D}}$ are size dependent [$\Delta G^{2\mathrm{D}}(m)$] and smaller than the bulk barrier [$\Delta G^{2\mathrm{D}}(m_{\mathrm{crit}}^{2\mathrm{D}})$]. The 2D critical island size $m_{\mathrm{crit}}^{2\mathrm{D}}$ is then given by:

$$\left.\frac{\partial \Delta G^{2\mathrm{D}}}{\partial m}\right|_{m_{\mathrm{crit}}^{2\mathrm{D}}} = \left[-\left(\frac{2m+1}{2}\right)\Delta\mu + (4\varepsilon_A + \varepsilon_S)\right]\Big|_{m_{\mathrm{crit}}^{2\mathrm{D}}} = 0\,. \tag{S8}$$

At fixed supersaturation, eq S8 defines the size-range of 2D islands exhibiting either size-dependent ($m < m_{\mathrm{crit}}^{2\mathrm{D}}$) or size-independent ($m \geq m_{\mathrm{crit}}^{2\mathrm{D}}$) barriers. Conversely, eq S8 also defines the 2D critical supersaturation ($\Delta\mu_{m,\mathrm{crit}}^{2\mathrm{D}}$) at which 2D islands of lateral size m dissolve:

$$\Delta\mu_{m,\mathrm{crit}}^{2\mathrm{D}} = \frac{2(4\varepsilon_A+\varepsilon_S)}{2m+1}\,. \tag{S9}$$

Like for the 3D critical size, the 2D critical size ($m_{\mathrm{crit}}^{2\mathrm{D}}$) and supersaturation ($\Delta\mu_{m,\mathrm{crit}}^{2\mathrm{D}}$) are inversely proportional.

Having defined the effect of supersaturation on the 2D and 3D critical size, we determine how the range of stable MSNCs exhibiting size-dependent barriers to the next-larger MSNC depends on supersaturation. We note that transitioning from MSNCs with n lateral monomers to the subsequent MSNCs requires the formation of a 2D surface island of $(n+1)$ monomers in lateral size. The barrier to transition from one MSNC to the next will only be size dependent if the required 2D surface island is smaller than the 2D critical size. In terms of supersaturation, this translates to the following condition:

$$\Delta\mu < \Delta\mu_{n+1,\mathrm{crit}}^{2\mathrm{D}}\,. \tag{S10}$$

MSNCs with n lateral monomers can only be stable and exhibit size-dependent barriers if the following inequality holds:

$$\Delta\mu_{n,\mathrm{crit}}^{3\mathrm{D}} < \Delta\mu_{n+1,\mathrm{crit}}^{2\mathrm{D}}\,. \tag{S11}$$

Then, a supersaturation regime exists where the MSNCs are stable ($\Delta\mu_{n,\mathrm{crit}}^{3\mathrm{D}} < \Delta\mu$) and exhibit size-dependent barriers to transition to the next-larger size ($\Delta\mu < \Delta\mu_{n+1,\mathrm{crit}}^{2\mathrm{D}}$). This regime is highlighted in beige for different-sized MSNCs in Figure 4a in the main text.

S3 MODEL PARAMETERS

The model presented above depends on two parameters only: the step energy (ε_S) and the energy of breaking a crystalline bond and passivating it with a ligand (ε_A). All calculations presented in the main

text have been performed using ε_A = 128 meV and $\varepsilon_S = 5\varepsilon_A$. In the following, we discuss how these parameters where chosen.

S3.1 Surface energy (ε_A)

The energy of breaking a crystalline bond and passivating it with a ligand (ε_A) is tightly linked to the surface energy (σ_A) of a passivated, Cd-terminated {111} facet. Here, we first discuss σ_A for unpassivated (bare) surfaces, and then incorporate the effect of ligands on σ_A.

Bare {111} facets have one dangling bond per monomer. For CdSe, their surface energy was reported to be 46 meV/Å^2 (Ko *et al.*[S5]) or 52 meV/Å^2 (Liu *et al.*[S6]). Ligands passivate dangling bonds and therefore reduce the surface energy of bare facets. This stabilizing effect strongly depends on the ligand type, on how it binds to the surface, and the surface coverage.[S5,S7] For passivated surfaces, σ_A is defined as:[S5]

$$\sigma_{A,p} = \sigma_{A,b} - \Delta\sigma_p \,, \tag{S12}$$

where $\sigma_{A,p}$ and $\sigma_{A,b}$ are the surface energies of the passivated ($\sigma_{A,p}$) and bare ($\sigma_{A,b}$) surfaces, and $\Delta\sigma_p$ quantifies the stabilizing effect of the passivating ligands. For Cd-terminated {111} facets passivated with acetate, Ko *et al.*[S5] report $\Delta\sigma_p$ to be 38 meV/Å^2 respectively. The surface energy of the passivated facet is then 8 meV/Å^2. Using 16 Å^2 for the surface area per dangling bond (ρ_A) yields 128 meV for ε_A, which is the value used in all of our calculations.

S3.2 Step energy (ε_S)

In our model, the step energy (ε_S) accounts for the fact that monomers located on the step edge cost an additional energy compared to monomers located on a terminated facet. This can occur because ligand passivation at the step front is different (*i.e.* less effective) compared to terminated facets, as proposed for CdSe nanoplatelets (NPLs).[S8] However, NPLs have Cd-rich {100} facets exposed, which is different compared to MSNCs, which have {111} facets exposed.

For {111} facets, no data on the step energy exists. In the absence of data, we determine ε_S (unknown) from ε_A (known) by imposing that $\Delta\mu^{3\mathrm{D}}_{n,\mathrm{crit}} < \Delta\mu^{2\mathrm{D}}_{n+1,\mathrm{crit}}$ holds for all MSNC sizes n. From this inequality we obtain the following condition on ε_S:

$$\varepsilon_S > \varepsilon_A \left(\frac{6(2n+3)(2n+1)}{3n^2+6n+2} - 4\right). \tag{S13}$$

For large n, ε_S is exactly four times larger than ε_A, while for n = 2, ε_S needs to be greater than 4.077ε_A. For the calculations reported in the main text, we chose $\varepsilon_S = 5\varepsilon_A$ to fulfill eq S13. Note that when ε_S is chosen such that that eq S13 is not fulfilled, no size regime of stable MSNCs exhibiting size-dependent barriers exists (see Figure S12). This will affect MSNC growth. However, we note that MSNCs are still local minima in the energy-of-formation curve.

S4 POPULATION-BALANCE MODEL

As MSNCs grow they incorporate monomers, which in turn reduces the monomer concentration in solution, c_1. The monomer concentration in solution is linked to the supersaturation as $\Delta\mu = k_B T \ln(c_1/c_\infty^*)$, where c_∞^* is the monomer concentration at the bulk solubility. In the main text we refer to c_1/c_∞^* as $\tilde{c}_1$. Intuitively, changes in $\tilde{c}_1$ depend on the growth and dissolution of MSNCs. At the same time, changes in $\tilde{c}_1$—and therefore also $\Delta\mu$—affect the growth rates of different MSNC populations, because the barriers to transition from one MSNC to the next-larger size vary (Figure 4b in the main text).

To include all these effects and simulate the temporal evolution of different MSNCs, we use a population-balance model. Experiments suggest that growth and dissolution occur layer by layer through the addition or removal of one monolayer. Therefore, we assume that each MSNC size can either grow to the next-larger MSNC (consuming monomers) or dissolve to the next-smaller MSNC (generating monomers). As a result, we describe the temporal change in concentration (c_n) of MSNC species of size $n \geq 2$ as:

$$\frac{d\tilde{c}_n}{dt} = I_{n-1}\tilde{c}_{n-1} + D_{n+1}\tilde{c}_{n+1} - (I_n + D_n)\tilde{c}_n \,, \tag{S14}$$

here given for the normalized concentrations $\tilde{c}_n = c_n/c_\infty^*$. Each of the four fluxes entering the right-hand side of eq S14 are given by both a concentration and a rate. The growth rate (I_i) depends on the supersaturation, the surface and step energies (ε_S, ε_A), the temperature (T), as well as the attempt frequency C. We define it as:

$$I_n = C\exp\left[-\frac{E_{n,\mathrm{barr}}}{k_B T}\right] \,;\; E_{n,\mathrm{barr}} = \begin{cases} \Delta G^{2\mathrm{D}}(n+1) + \varepsilon_S(n+1) & \text{if } n+1 \leq m_{\mathrm{crit}}^{2\mathrm{D}} \\ \Delta G^{2\mathrm{D}}\left(m_{\mathrm{crit}}^{2\mathrm{D}}\right) & \text{if } n+1 > m_{\mathrm{crit}}^{2\mathrm{D}} \end{cases}. \tag{S15}$$

We distinguish two cases in eq S15 because MSNCs that have to grow facets smaller than the 2D critical island size ($m_{\mathrm{crit}}^{2\mathrm{D}}$) exhibit size-dependent barriers to transition to the next-larger MSNCs. To correctly compute the barriers ($E_{n,\mathrm{barr}}$), we need to explicitly include the step-energy term $[\varepsilon_S(n+1)]$ for $n + 1 \leq m_{\mathrm{crit}}^{2\mathrm{D}}$. Otherwise, this term would be missing due to the definition of $\Delta G^{2\mathrm{D}}(n+1)$ in eq S5. The dissolution rates (D_i) are defined by imposing the equilibrium condition. Namely, at the critical supersaturation $\Delta\mu_{n,\mathrm{crit}}^{3\mathrm{D}}$, the rate of forming a MSNC of lateral size n (I_{n-1}) has to be the same as the rate of dissolution (D_n):

$$D_n = I_{n-1}(\Delta\mu_{n,\mathrm{crit}}^{3\mathrm{D}}) \,. \tag{S16}$$

Finally, temporal changes in the monomer concentration in solution, $\tilde{c}_1$, are accounted for by imposing mass balance on the overall system. In differential form this reads as:

$$\frac{d\tilde{c}_1}{dt} = -\sum_{n\geq 2}^{N} \Phi(n)\frac{d\tilde{c}_n}{dt} \,, \tag{S17}$$

where N is the largest size considered. In principle, N should be infinite. In practice, N has to be finite. In our simulations it is chosen to be 30, which is large enough not to have any effect on the growth dynamics. For the largest size considered, we neglect the $D_{N+1}\tilde{c}_{N+1}$ term in eq S14.

The master equations (eq S14 and S17) determine the temporal evolution of our system. They constitute a system of non-linear ordinary differential equations, which we solve using the high-performance Python compiler Numba. In all our simulations we assume the temperature to be 200 °C, and an attempt frequency of $1\text{x}10^{17}$. The attempt frequency which has units of s^{-1} defines the normalized time $\tau = Ct$. For the initial supersaturation in our simulations we assumed a value of 550 meV (which is larger than $\Delta\mu_{2,\mathrm{crit}}^{3\mathrm{D}}$). Increasing the initial supersaturation reduces the times at which small sizes ($n \leq 4$) are observed. However, we find that it has no substantial impact on the overall MSNC growth dynamics.

S5 SUPPORTING FIGURES

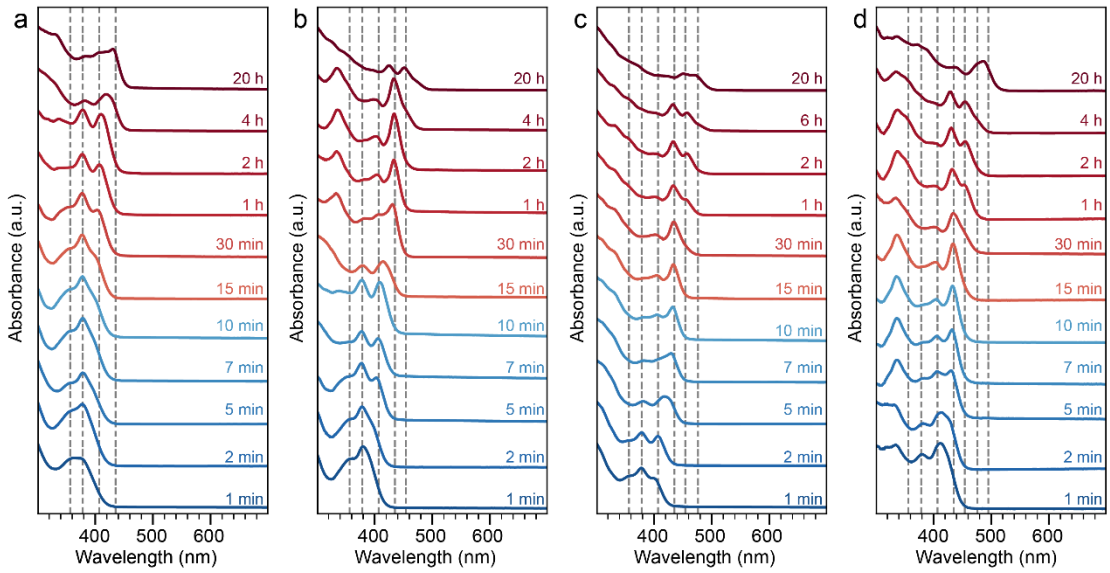

Figure S1. Temporal evolution of optical absorption spectra of CdSe MSNCs grown at different temperatures: (**a**) 120 °C, (**b**) 150 °C, (**c**) 180 °C, and (**d**) 210 °C. Each spectrum is labelled with the time after injection. The vertical dashed lines indicate the lowest energy excitonic peaks for MSNC product species (at 355, 380, 408, 434, 455, 476, 494, 508, and 523 nm). As we increase the growth temperature, the observed range of discrete excitonic features shifts from shorter to longer wavelengths.

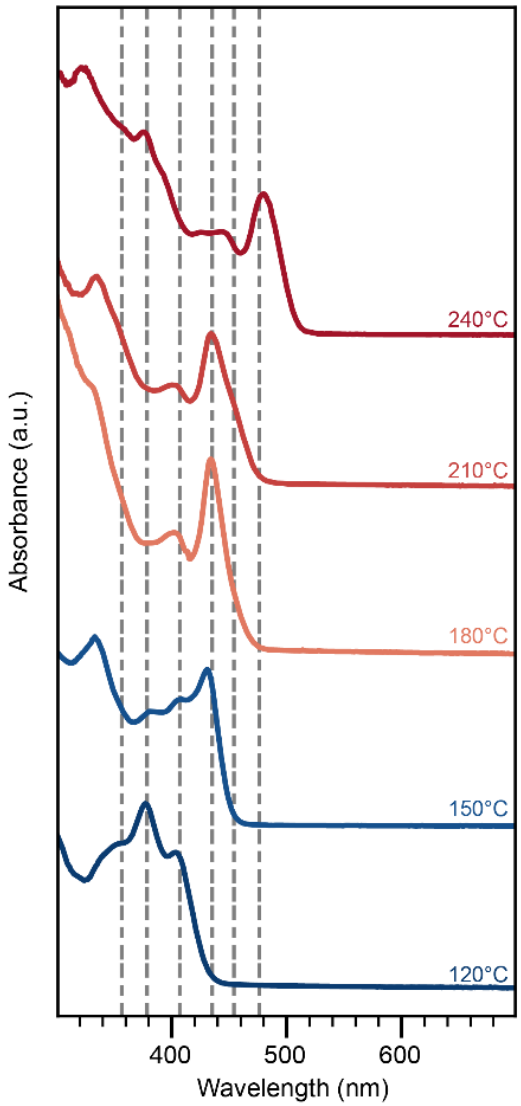

Figure S2. Effect of growth temperature on the synthesis of CdSe MSNCs. Optical absorption spectra of aliquots taken 30 min after the injection of bis(stearoyl) selenide at different temperatures. Each spectrum is labelled with the injection and growth temperature. Higher injection and growth temperatures result in faster discrete and sequential transitions to absorption features at longer wavelengths.

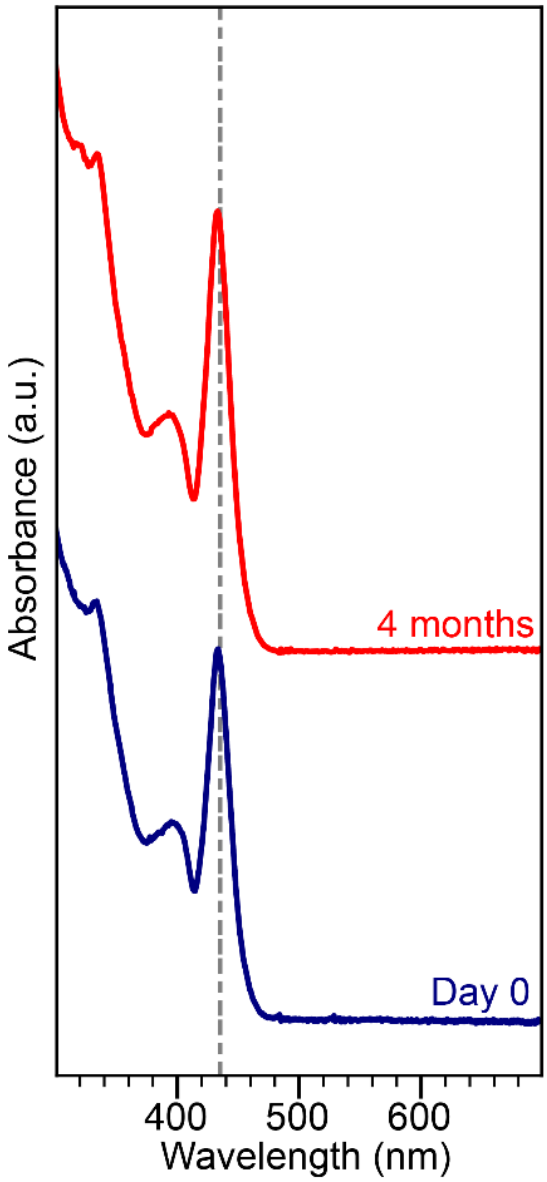

Figure S3. Stability of CdSe MSNCs under ambient conditions. Optical absorption spectra of isolated 434 immediately after the synthesis (blue) and after 4 months (red). The products were stored under ambient conditions as a liquid dispersion in hexane (optical density at the lowest energy excitonic transition >1.5 for a 1-cm path length).

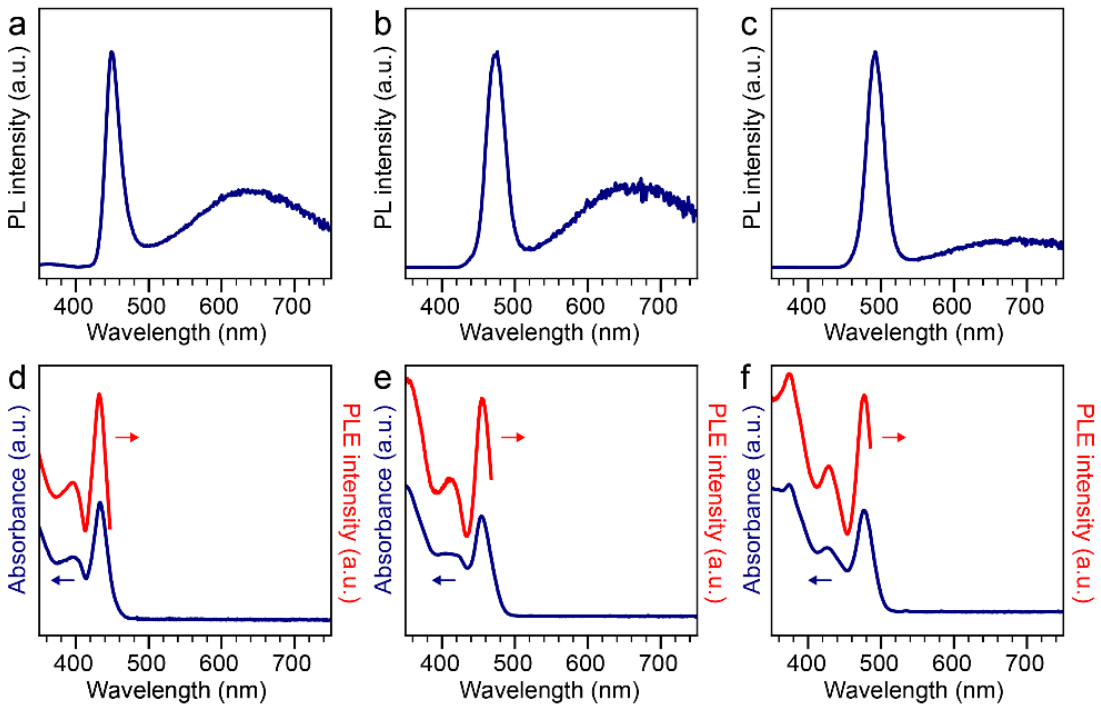

Figure S4. Optical characterization of isolated CdSe MSNCs. Room-temperature photoluminescence (PL) spectra of the isolated (a) 434, (b) 455, and (c) 476 species. For PL, the excitation wavelength is 300 nm. Room-temperature photoluminescence excitation (PLE, red) and absorption (blue) spectra of the isolated (a) 434, (b) 455, and (c) 476 species. For PLE, the emission is monitored at 452, 472, and 490 nm, respectively.

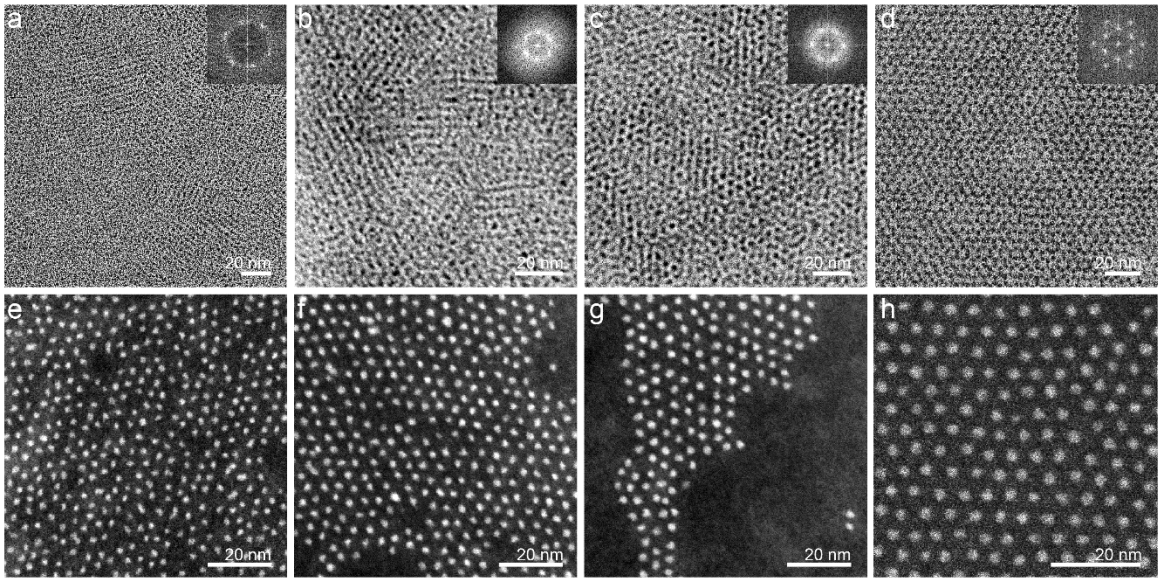

Figure S5. Electron microscopy images of isolated CdSe MSNC species. The transmission electron microscopy (TEM) images at lower magnification and the corresponding fast-Fourier transforms (FFT) (inset right) are shown for: (a) 434, (b) 455, (c) 476, and (d) 494 species. The formation of assemblies of MSNCs suggests uniform particles. High-angle annular dark-field (HAADF) scanning transmission electron microscopy (STEM) images of (e) 434, (f) 455, (g) 476, and (h) 494 species reveal no sign of molecular templates.

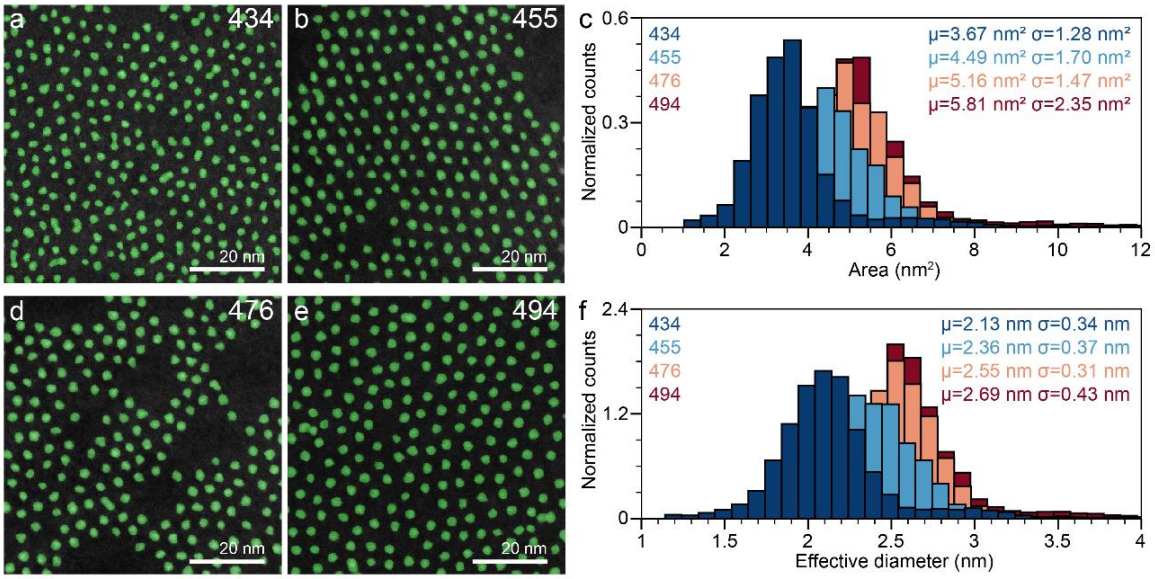

Figure S6. Size analysis of CdSe MSNCs using transmission electron microscopy. Images show detected objects (green) after evaluating the high-angle annular dark-field (HAADF) scanning transmission electron microscopy (STEM) images of (a) 434, (b) 455, (d) 476, and (e) 494 species using a custom Python script. (c) Normalized histograms with mean (μ) and standard deviation (σ) of the area of the detected objects. (f) The extracted effective diameter. The bin sizes of histograms in (c) and (f) are 0.4 nm^2 and 0.1 nm, respectively. A total of 21,275 (434), 12,143 (455), 9,915 (476), and 14,767 (494) particles were analyzed. The mean areas and effective diameters increase, consistent with the discrete jumps observed in the optical spectra (see Figure 1a in the main text). We note that while strategies to minimize electron-beam damage in the STEM images were followed (see Section S1.3), the images are still potentially affected. See also Figure S7.

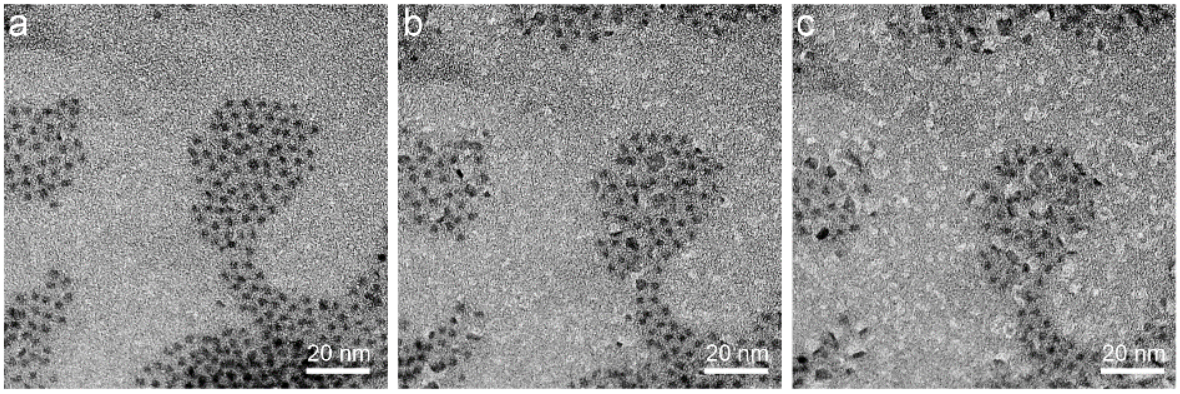

Figure S7. Shape evolution and damage induced by the electron beam for CdSe MSNCs. The transmission electron micrographs are at a magnification of 300k for isolated 494. The sample was fixed at a particular position and exposed to the 120 kV beam for a few minutes. The images were recorded at (a) 0 min, (b) 2 min, and (c) 4 min. The drift induced at higher magnification slightly shifts the position of the sample over time. The rate of beam-induced damage increases at higher magnifications.

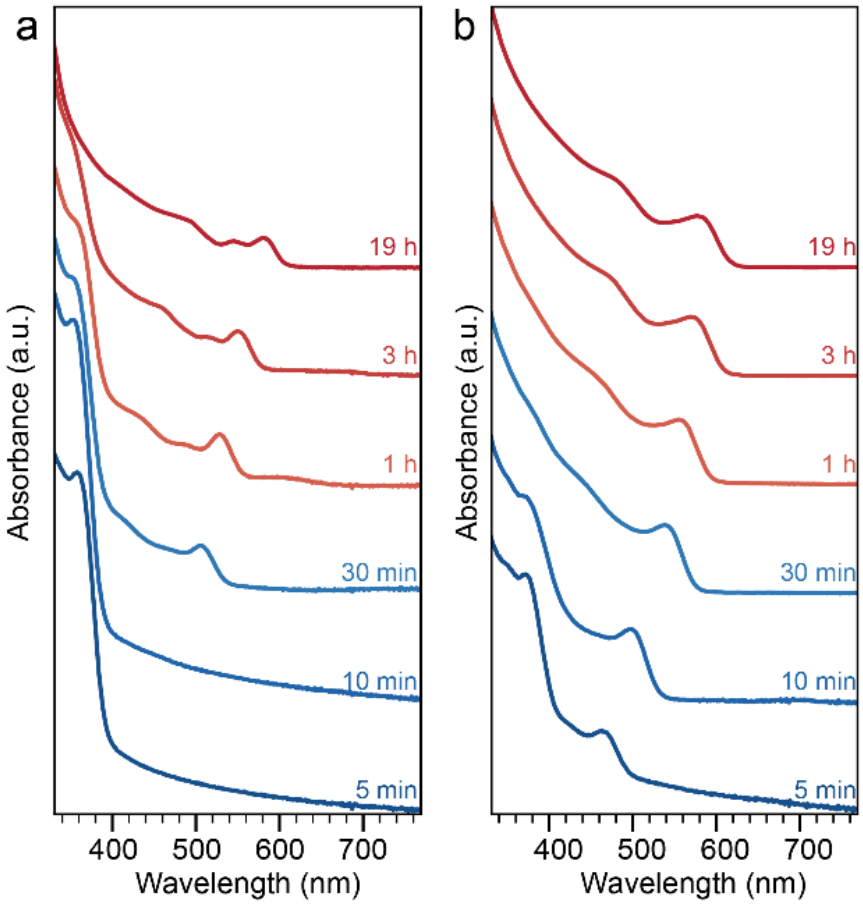

Figure S8. Replacing the reactive Se precursor in CdSe MSNC synthesis with less reactive precursors. Temporal evolution of optical absorption spectra when the Se precursor, bis(stearoyl) selenide, was replaced with equimolar (a) elemental selenium or (b) trioctylphosphine selenide. Each spectrum is labelled with the injection and growth time. The absence of discrete and sequential evolution of excitonic features suggests that magic-sized nanocrystals have not been formed.

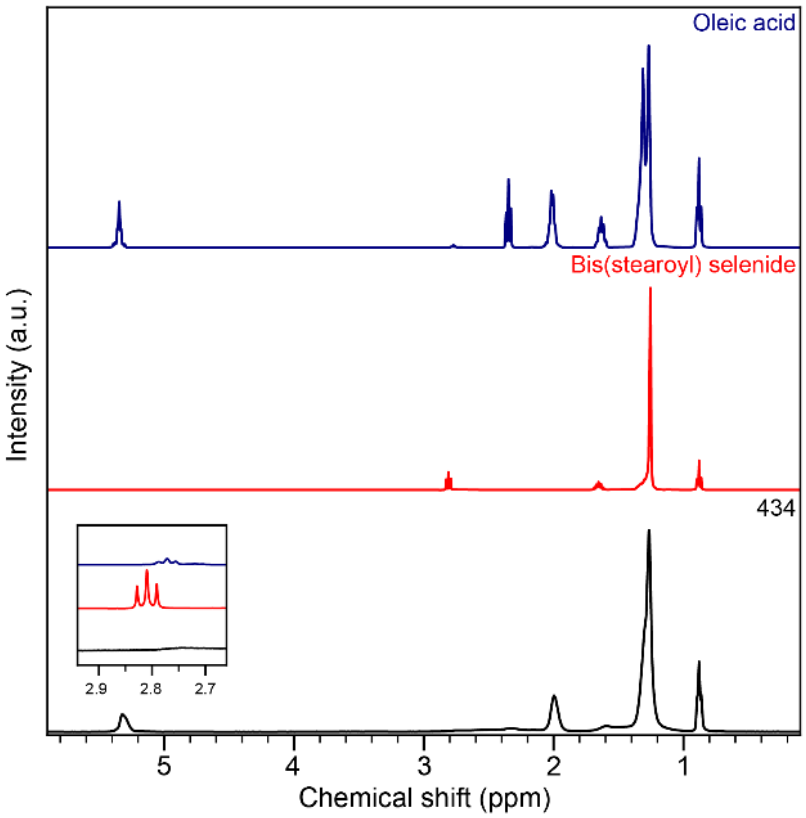

Figure S9. Nuclear magnetic resonance spectrum of isolated CdSe MSNC 434. ^{1}H NMR spectra (400 MHz) of isolated 434 (black), bis(stearoyl) selenide (red), and pure oleic acid (blue) in $CDCl_3$. The broadness of the peaks in the spectrum of 434 is presumably due to the restricted movement of ligands when they are attached to the crystallite surface. The absence of a peak at 2.81 ppm (inset) suggests the absence of the bis(stearoyl) selenide precursor in the isolated 434. Furthermore, the peaks of 434 were quantitatively integrated. The ratios of the intensities of the different peaks match the ratios in the oleic acid molecule. This supports the existence of only one molecule (the ligand) in the system ensuring complete isolation of MSNC from the selenium precursors.

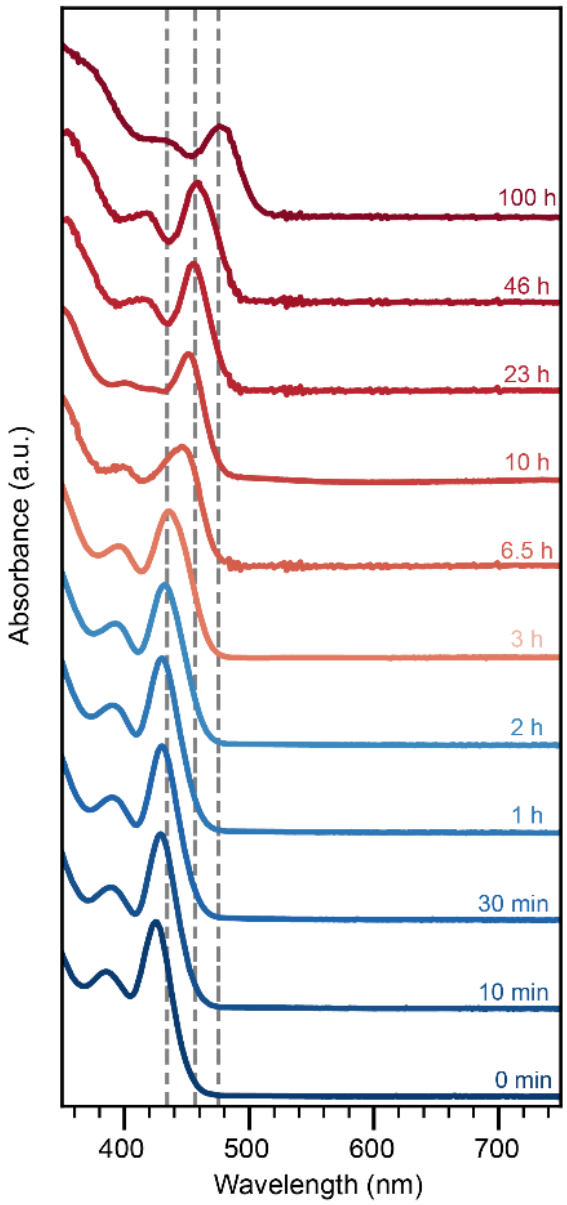

Figure S10. Growth of isolated CdSe MSNC 434 without selenium and cadmium precursors. Temporal evolution of the optical absorption spectra of the isolated 434 heated in ODE at 180 °C. Each spectrum is labelled with the growth time. The vertical dashed lines indicate the lowest energy excitonic peaks for 3 MSNCs (at 434, 455, and 476 nm). Discrete growth is not observed.

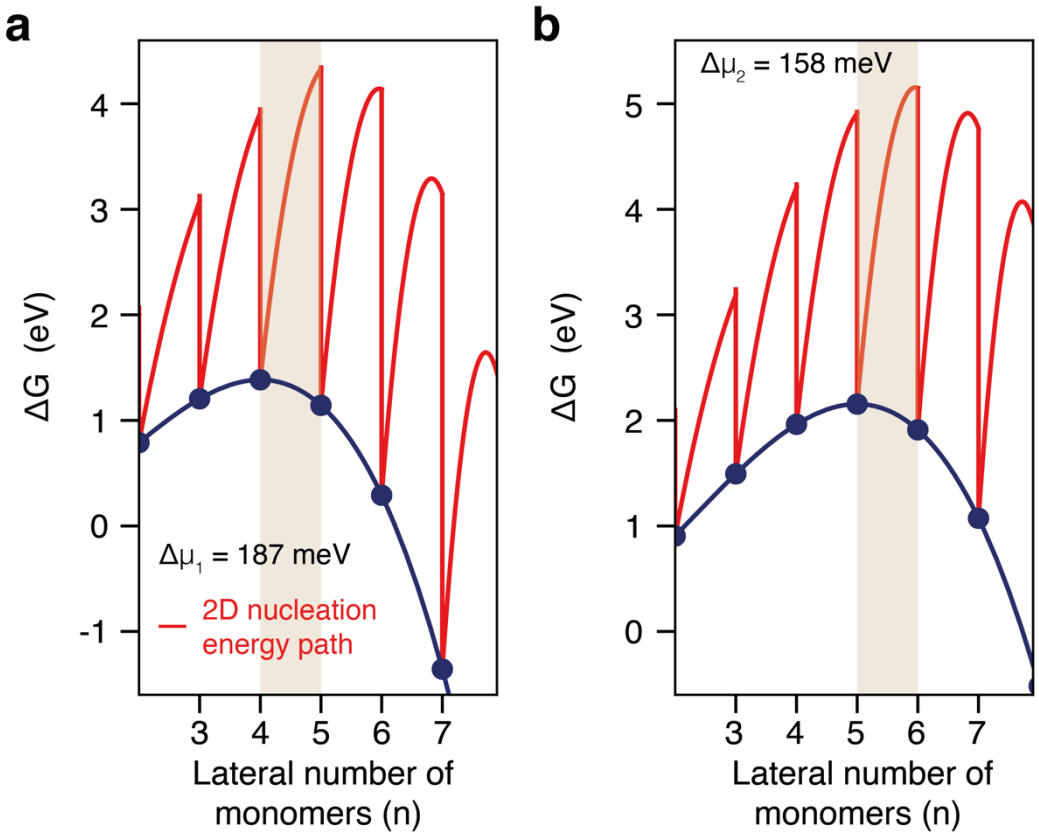

Figure S11. Free energy of formation for different-sized MSNCs for two different fixed supersaturations ($\Delta\mu$). (a,b) The total free energy of different sizes of MSNCs (blue dots) and the transition states (red lines) that link them are plotted for different supersaturations [$\Delta\mu$ in (a) is larger than in (b)]. As the supersaturation decreases, the barriers linking different MSNC sizes increase. Simultaneously, the size range of stable MSNCs exhibiting size-dependent barriers (highlighted in beige) shifts to larger MSNC sizes.

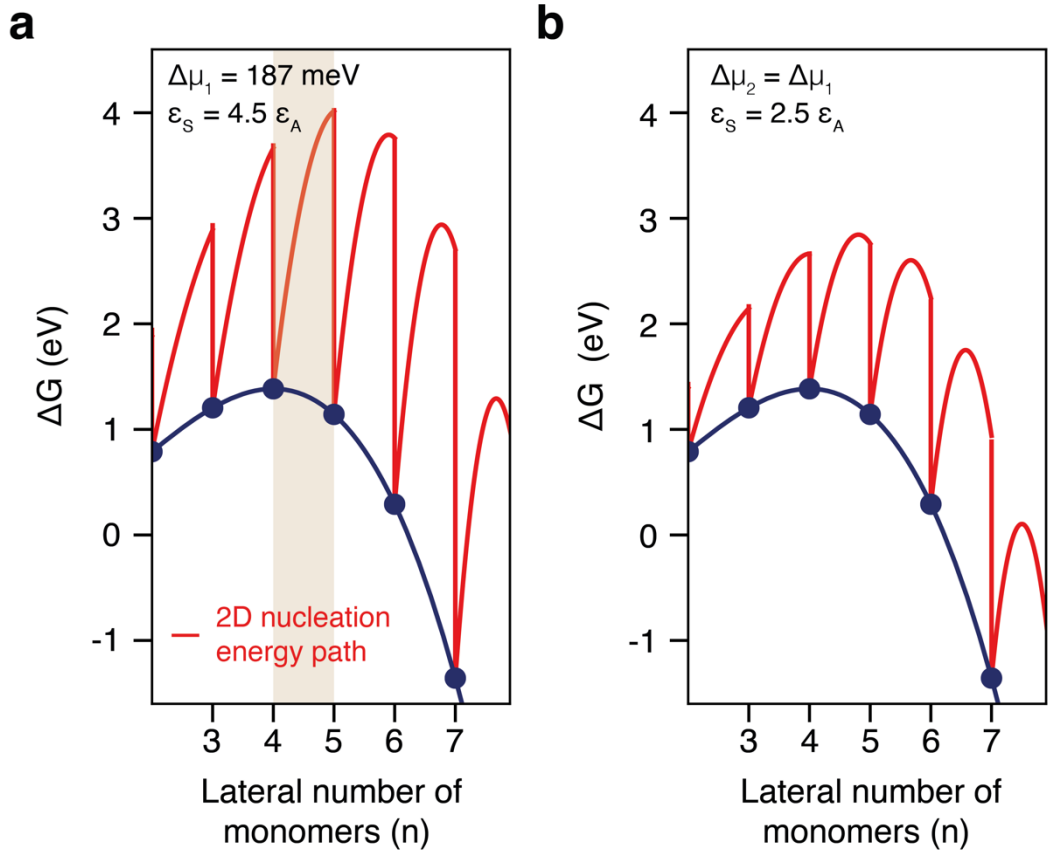

Figure S12. Free energy of formation for different-sized MSNCs for different model parameters. (a,b) Total free energy of different sizes of MSNCs (blue dots) and the transition states (red lines) that link them are plotted for (a) $\varepsilon_S = 4.5\varepsilon_A$ and (b) $\varepsilon_S = 2.5\varepsilon_A$. The supersaturation and surface energy, ε_A, is the same in both plots. Changes in ε_S do not affect the absolute stability of MSNCs (eq S7), they only affect the barriers linking different sizes (eq S9). When ε_S does not fulfill the inequality given in eq S13 [as in (b) where $\varepsilon_S = 2.5\varepsilon_A$], no size-regime exists for stable MSNCs exhibiting size-dependent barriers. However, MSNCs still correspond to local minima in the energy-of-formation curve.

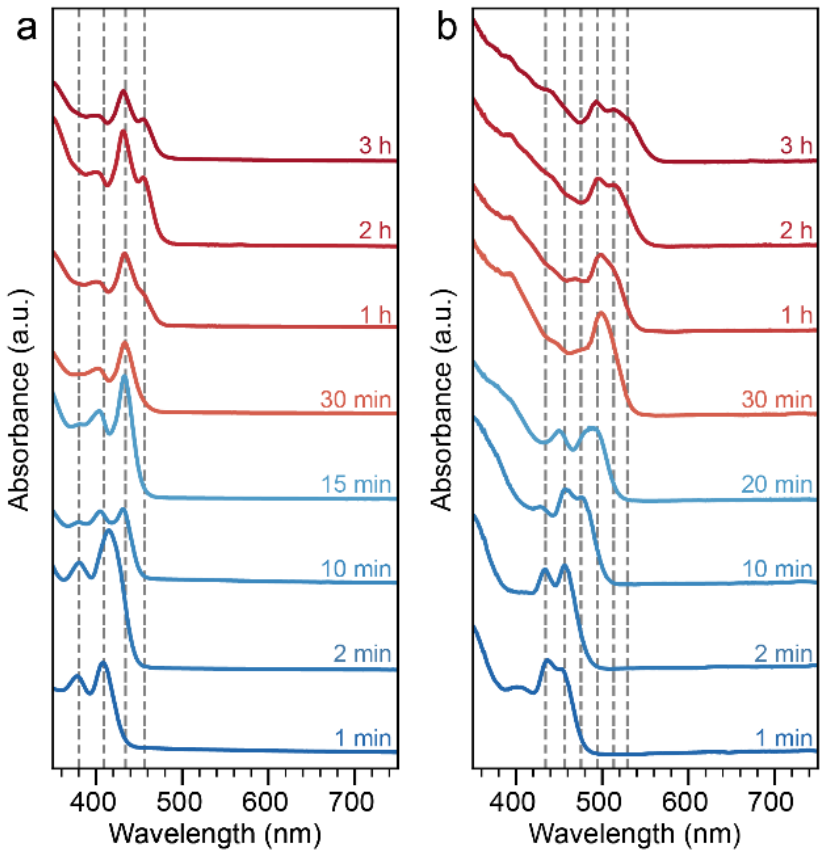

Figure S13. Temporal evolution of optical absorption spectra for CdSe MSNC growth in the presence or absence of chlorides. CdSe MSNCs are grown at 180 °C (a) without and (b) with cadmium chloride. Each spectrum is labelled with the time after the injection. The vertical dashed lines for the synthesis without chloride indicate the lowest energy excitonic peaks for 4 MSNC species (at 380, 408, 434, and 455 nm). The vertical dashed lines for the synthesis with chloride indicate the lowest energy excitonic peaks for 7 MSNC species (at 408, 434, 455, 476, 494, 512, and 528 nm). The observation of larger species with chloride indicates faster growth of MSNCs. We note that a slight red shift occurs for the spectral position of the absorption peaks of the larger MSNC sizes when chloride is present (512 *versus* 508 nm and 528 *versus* 523 nm).

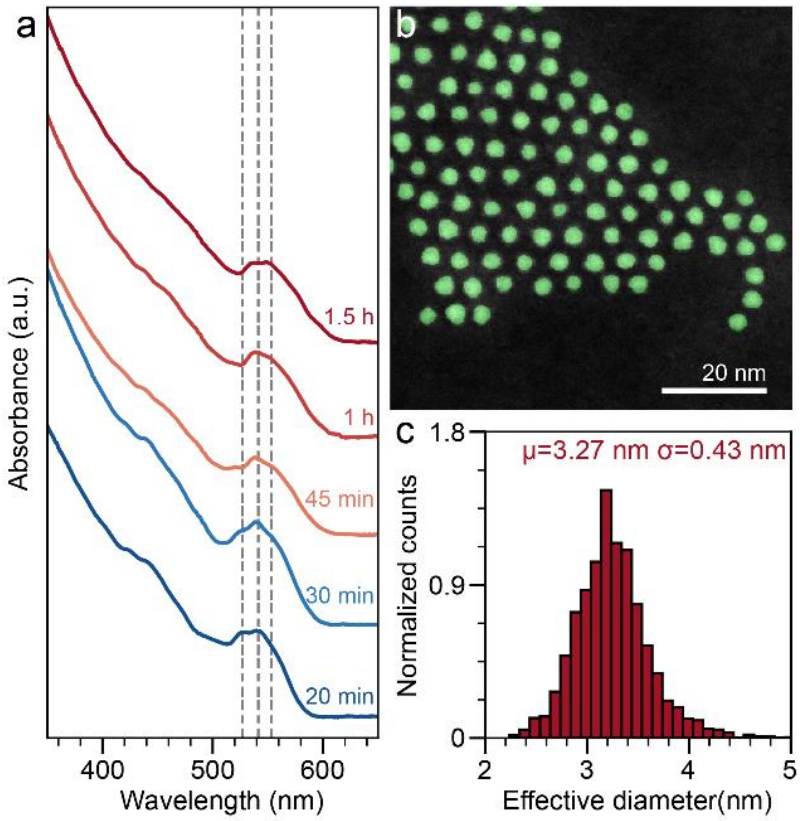

Figure S14. Optical characterization and size analysis of CdSe MSNCs grown in the presence of chlorides. (a) Temporal evolution of the optical absorption spectra of CdSe MSNCs grown at 240 °C in the presence of chloride. Each spectrum is labelled with the time after injection. The vertical dashed lines indicate the lowest energy excitonic peaks for 3 MSNC product species (at 528, 542, and 554 nm). At least two new MSNC species were observed. We note that a slight red shift occurs for the spectral position of the absorption peaks of the larger MSNC sizes when chloride is present (528 *versus* 523 nm). See also Figure S13. (b) Image shows detected objects (green) after evaluating the high-angle annular dark-field (HAADF) scanning transmission electron microscopy (STEM) images of 554 species using a custom Python script. (c) Normalized histogram with the mean (μ) and standard deviation (σ) of the extracted effective diameter of the 554 species. A total of 4,517 particles were analyzed. The bin size of the histogram is 0.1 nm.

S6. SUPPORTING REFERENCES

(S1) Hendricks, M. P.; Campos, M. P.; Cleveland, G. T.; Jen-La Plante, I.; Owen, J. S. A Tunable Library of Substituted Thiourea Precursors to Metal Sulfide Nanocrystals. *Science* **2015**, *348*, 1226–1230.

(S2) Koketsu, M.; Nada, F.; Hiramatsu, S.; Ishihara, H. Reactions of Acyl Chlorides with LiAlHSeH. Preparation of Diacyl Selenides, Diacyl Diselenides, Selenocarboxylates and Cyclic Selenoanhydrides. *J. Chem. Soc., Perkin Trans. 1* **2002**, No. 6, 737–740.

(S3) Beecher, A. N.; Yang, X.; Palmer, J. H.; Lagrassa, A. L.; Juhas, P.; Billinge, S. J. L.; Owen, J. S. Atomic Structures and Gram Scale Synthesis of Three Tetrahedral Quantum Dots. *J. Am. Chem. Soc.* **2014**, *136*, 10645–10653.

(S4) Kudera, S. Formation of Colloidal Semiconductor Nanocrystals: The Aspect of Nucleation, Ph. D. Thesis, Ludwig-Maximilians-Universität München, Munich, October 2007.

(S5) Ko, J. H.; Yoo, D.; Kim, Y. H. Atomic Models for Anionic Ligand Passivation of Cation-Rich Surfaces of IV-VI, II-VI, and III-V Colloidal Quantum Dots. *Chem. Commun.* **2017**, *53*, 388–391.

(S6) Liu, L.; Zhuang, Z.; Xie, T.; Wang, Y.-G.; Li, J.; Peng, Q.; Li, Y. Shape Control of CdSe Nanocrystals with Zinc Blende Structure. *J. Am. Chem. Soc.* **2009**, *131*, 16423–16429.

(S7) Bealing, C. R.; Baumgardner, W. J.; Choi, J. J.; Hanrath, T.; Hennig, R. G. Predicting Nanocrystal Shape through Consideration of Surface-Ligand Interactions. *ACS Nano* **2012**, *6*, 2118–2127.

(S8) Riedinger, A.; Ott, F. D.; Mule, A.; Mazzotti, S.; Knüsel, P. N.; Kress, S. J. P.; Prins, F.; Erwin, S. C.; Norris, D. J. An Intrinsic Growth Instability in Isotropic Materials Leads to Quasi-Two-Dimensional Nanoplatelets. *Nat. Mater.* **2017**, *16*, 743–748.